ELSEVIER

Contents lists available at ScienceDirect

Energy Storage Materials

journal homepage: www.elsevier.com/locate/ensm



Comprehensive study of Mn/Ni ordering in LiNi_{0.5-x}Mn_{1.5+x}O₄ using neutron powder diffraction and scanning transmission electron microscopy

Ilia Tertov ^{a,b,c}, Dmitry Chezganov ^d, Emmanuelle Suard ^a, Mylène Hendrickx ^e, Thomas Hansen ^a, François Fauth ^f, François Weill ^{b,g}, Pierre-Etienne Cabelguen ^e, Christian Masquelier ^{c,g,h,*}, Laurence Croguennec ^{b,g,*}

- ^a Institut Laue-Langevin, F-38042, Grenoble, France
- b Univ. Bordeaux, CNRS, Bordeaux INP, ICMCB UMR 5026, F-33600, Pessac, France
- c Laboratoire de Réactivité et de Chimie des Solides, Université de Picardie Jules Verne, CNRS-UMR 7314, F-80039, Amiens Cedex 1, France
- ^d EMAT, University of Antwerp, BE-2020, Antwerp, Belgium
- e Umicore, 31 rue du marais, Brussels BE-1000, Belgium
- f CELLS-ALBA Synchrotron, Cerdanyola del Vallès, E-08290 Barcelona, Spain
- g RS2E, Réseau sur le stockage électrochimique de l'énergie, FR CNRS 3459, F-80039, Amiens Cedex 1, France
- ^h Institut Universitaire de France, 103 boulevard Saint-Michel, F-75005 Paris, France

ARTICLE INFO

Keywords: In situ neutron powder diffraction Scanning transmission electron microscopy Cation ordering LNMO

ABSTRACT

In this study, we extensively establish unique relationships between the chemical compositions of LiNi $_{0.5}$ _xMn $_{1.5+x}$ O₄ (LNMO) spinel-type positive electrode materials and the degree of Mn/Ni ordering, which influences their electrochemical performance. To achieve this, *in situ* temperature-controlled neutron powder diffraction experiments were performed under air or oxygen atmospheres to track the Mn/Ni ordering process during annealing of LNMO samples that contain different Mn/Ni ratios. Systematic in-depth structural analysis of a large number of samples, using both neutron and synchrotron X-ray powder diffractions, revealed clear correlations between the variations in the voltage-composition profiles and the distribution of Mn and Ni atoms between the 4b and 12d crystallographic sites of ordered LNMO. Additionally, we employed high-resolution scanning transmission electron microscopy combined with fast Fourier transform analysis that enabled us to visualize the distribution and sizes of Mn/Ni ordered domains at the particle level in excellent agreement with the Rietveld refinement from neutron powder diffraction data.

1. Introduction

 $LiNi_{0.5}Mn_{1.5}O_4$ (LNMO) is recognized as a highly promising spinel-type positive electrode material for Li-ion batteries (LIBs). Its high operating voltage of 4.8 V *versus* Li⁺/Li, driven by the Ni⁴⁺/Ni³⁺/Ni²⁺ redox couples, offers a significant energy density, which is essential for developing next-generation LIBs [1].

LNMO crystallizes with varying degrees of Mn/Ni ordering. The disordered LNMO phase, typically obtained by annealing at temperatures above 730 °C under air, is described by a face-centered cubic structure ($Fd\overline{3}m$ S.G.), into which Li atoms occupy the 8a tetrahedral sites, and Mn and Ni atoms share the 16d octahedral sites. In the ordered phase, obtained by annealing at lower temperatures [2–4], the symmetry lowers to a primitive cubic cell ($P4_332$ S.G.), with Li, Ni, and Mn

atoms occupying the 8c, 4b, and 12d sites, respectively.

During the synthesis of LNMO materials, oxygen release begins at T \geq 700 °C in air and at T \geq 720 °C in an oxygen atmosphere, leading to the formation of a rock salt-type impurity phase, commonly through a two-stage solid-state method [1]. Reversibly, annealing at lower temperatures, typically in the range of 600–700 °C, promotes oxygen intake, reducing the amount of the rock salt impurity, and fostering the formation of the ordered LNMO spinel phase. Cabana et al. [5], using transmission electron microscopy (TEM) combined with energy-dispersive X-ray analysis, showed that the rock salt impurity domains have a Mn/Ni ratio of 2:1, compared to the Mn/Ni ratio of 3:1 in the LNMO stoichiometric targeted spinel phase. In other words, the formation of the rock salt phase leads to Mn enrichment in the LNMO spinel phase, forming LiNi_{0.5-x}Mn_{1.5+x}O₄. Summarizing the literature

E-mail addresses: christian.masquelier@u-picardie.fr (C. Masquelier), laurence.croguennec@icmcb.cnrs.fr (L. Croguennec).

^{*} Corresponding authors.

data, we can express the equilibrium between the disordered and ordered spinel phases in LNMO samples with the following equation:

$$\begin{array}{c} LiNi_{0.5}Mn_{1.5}O_4 \leftrightarrow qLiNii_{0.5-x}Mn_{1.5+x}O_4 + pLi_{1-y}(Ni_zMn_{1-z})_{1+y}O_2 + tO_2 \uparrow \\ \text{Ordered} \end{array} \tag{1}$$

It can be hypothesized that the driving force behind the phase transition from the ordered to the disordered phase is the increased amount of Mn. Indeed, while in the ideal structure of LiNi_{0.5}Mn_{1.5}O₄, only Ni²⁺ and Mn⁴⁺ cations are present, Mn³⁺ cations are introduced for charge compensation, when the Mn content in the LNMO spinel phase increases due to the formation of impurities (Eq. (1)). These Mn³⁺ cations have a larger ionic radius (0.65 Å, CN = 6) compared to Mn⁴⁺ cations (0.53 Å, CN = 6), which may promote disordering.

Besides X-ray powder diffraction, Fourier-transformed infrared (FTIR), Raman or 7 Li magic angle spinning (MAS) NMR spectroscopies [6-8], the most powerful method for quantitative analysis of Mn/Ni ordering is neutron powder diffraction (NPD), thanks to the significant difference in neutron coherent scattering lengths between Ni and Mn: 10.3 fm and -3.7 fm, respectively. This allows the quantitative determination of the distribution of Mn and Ni between the 4b and 12d sites of ordered LNMO. In a seminal work by Casas-Cabanas et al. [9], it was proposed that at the particle level, nano-sized antiphase ordered domains form, the size of which being calculated from the broadening of the superstructure reflections. Casas-Cabanas et al. [9] and Kim et al. [10] additionally concluded that samples with small ordered domain sizes (10-20 nm) showed the most attractive electrochemical properties and demonstrated that for ordered domains of the same size, the mixing of Ni and Mn between the 4b and 12d sites improved the performance at high charge-discharge rates. In the work of Kim et al. [10], transmission electron microscopy imaging coupled with fast Fourier transform revealed that within a single particle, regions corresponding to both ordered and disordered LNMO spinel phases coexisted, suggesting that Mn/Ni ordering may occur heterogeneously at the particle level, with predominance of disordered domains near the particle surface.

In a recent study by Aktekin et al. [11], the authors used in situ temperature-controlled NPD under oxygen to show that Mn/Ni disordering in the Mn-rich LNMO sample with Mn/Ni = 78/22 (LiNi_{0.44}Mn_{1.56}O₄) begins at $T \approx 630$ °C, well below the temperature at which oxygen loss starts, thus suggesting that disordered LNMO samples could be prepared without side impurity phases. A possible reason for this behavior could be the slight excess of Mn, which would facilitate Mn/Ni disordering. These results contradict the findings of Kunduraci et al. [4], who studied a series of Mn-rich LNMO samples, LiNi_xMn_{2-x}O₄ $(0.36 \le x \le 0.5)$, and used FTIR to demonstrate the formation of ordered LNMO in samples with $x \ge 0.38$ at $T \le 700$ °C. It is worth noting that Cai et al. [3], also using in situ temperature-controlled NPD under air, did not observe Mn/Ni disordering at $T \le 700$ °C for an LNMO sample with Mn/Ni = 75/25. Moreover, in a recent study by Emery et al. [12], using NPD, the formation of the ordered LNMO spinel phase for a series of samples with $x \ge 0.38$ in LiNi_xMn_{2-x}O₄ was clearly demonstrated.

These conflicting results reported in the literature motivated us to conduct a systematic investigation into the influence of the Mn/Ni ratio on Mn/Ni ordering in LNMO materials. In fact, a lot of questions remain open regarding how Mn and Ni ordering occurs at the particle level, whether these ordered domains exist, and how they are distributed within a single particle. In one of our previous studies, we successfully prepared samples with similar Mn content in the LNMO spinel phase but with significantly different ordered domain sizes, from 7 to 56 nm. Our results suggest that it is the Mn content in the LNMO spinel phase, rather than the size of the ordered domains, that determines the material's performance at high charge-discharge rates [13]. The most promising properties are exhibited by materials with a slight excess of Mn in the LNMO spinel phase. We decided to focus on stoichiometric (Mn/Ni = 75/25) and Mn-rich (Mn/Ni = 77/23) LNMO samples.

In this study, we extensively used in situ temperature-controlled NPD

under both air and oxygen atmospheres to track the Mn/Ni ordering process during the annealing of LNMO samples and hence obtained a large series of samples with varying degrees of Mn/Ni ordering. The structural analysis of these samples using both NPD and synchrotron X-ray powder diffraction (SXRPD) allows us to correlate changes in the shape of the charge-discharge voltage-composition profiles with changes in the distribution of Mn and Ni atoms between the 4b and 12d sites. Additionally, we propose a novel method using high-resolution scanning transmission electron microscopy coupled with fast Fourier transform (FFT), which enabled us to illustrate Mn/Ni ordering at the particle level and correlate these data with the results of Rietveld refinements of NPD data.

2. Experimental section

2.1. Synthesis

The pristine LiNi $_{0.5}$ Mn $_{1.5}$ O $_4$ and LiNi $_{0.46}$ Mn $_{1.54}$ O $_4$ samples were prepared from the mixtures of (i) Li $_2$ CO $_3$ and Ni $_{0.25}$ Mn $_{0.75}$ (OH) $_2$ (Mn/Ni = 75/25), (ii) Li $_2$ CO $_3$ and Ni $_{0.23}$ Mn $_{0.77}$ (OH) $_2$ (Mn/Ni = 77/23) by firing at T = 1050 °C for 12 h under an air atmosphere. The heating rates were set to 5 °C/min until 500 °C followed by 1 °C/min until 1050 °C. Then the samples were cooled down to room temperature over 8 h. From the pristine samples, series of 77/23 Air, 77/23 Oxygen, 75/25 Air and 75/25 Oxygen samples were prepared for advanced structural investigations. They were obtained by annealing the pristine LiNi $_{0.46}$ Mn $_{1.54}$ O $_4$ (77/23) and LiNi $_{0.5}$ Mn $_{1.5}$ O $_4$ (75/25) samples in air or oxygen atmospheres for 12 h at temperatures of 625, 650, 675, 700, and 725 °C. The heating rates were set to 5 °C/min up to 500 °C followed by 1 °C/min up to the set temperature. The cooling rate was set to 5 °C/min until room temperature. The sample names are composed of the series name and the annealing temperature, for example, "77/23 Air 625 °C".

2.2. Materials characterization

The D20 beamline (Institut Laue-Langevin, France) was used to perform *in situ* temperature-controlled NPD experiments with a wavelength of 1.54 Å. Approximately 3 g of the pristine 77/23 and 75/25 samples were placed in the middle of the two-end-open quartz tube with outer diameter of 12 mm and inner diameter of 8 mm. To ensure a good contact with the gas atmosphere, a flow of synthetic air or oxygen was circulating through the sample. The sample was heated in the D20's dedicated furnace equipped with a vanadium heating element, the heating rates being of 5 °C/min up to 500 °C and then of 1 °C/min up to set temperature, depending on the experiment. The collection time of the NPD patterns was 1 min for the 77/23 Air experiment, and 2 min for the 77/23 Oxygen and 75/25 Air experiments.

SXRPD patterns from samples sealed in 0.7 mm diameter borosilicate glass capillaries were collected using the BL04-MSPD beamline (ALBA, Spain) [14] with a wavelength of 0.6206 Å and 0.6362 Å, using the position sensitive MYTHEN II detector in Debye-Scherrer geometry. High-angular resolution SXRPD measurements were performed on the BL04-MSPD with a wavelength of 0.41377 Å using the MAD setup [14]. High-angular resolution NPD patterns were collected on the D2B beamline (Institut Laue-Langevin, France) with a wavelength of 1.59 Å in Debye–Scherrer geometry. The instrumental profile function of both SXRPD and NPD diffractometers was determined using Na₂Ca₃Al₂F₁₄ as a standard sample. Treatment of diffraction data and Rietveld refinements were performed using the FullProf suite software packages [15]. Additional Lorentzian broadening observed for superstructure reflections of ordered LNMO ($P4_3$ 32 S.G.), present as signature of small antiphase domains, was refined with FullProf using size model #-2.

The 77/23 Air 625 °C, 77/23 Air 650 °C, 77/23 Air 675 °C and 77/23 Air 700 °C samples were analyzed using high-resolution scanning transmission electron microscopy (HR-STEM) to examine the ordered domain distribution. For the study, the lamellae were prepared using the

focused ion beam (FIB) technique on powder samples deposited on a carbon tape. After applying a 25-nanometer carbon coating, the surface of the particles was coated with platinum using electron and ion beam deposition in the FEI Helios NanoLab 650 DualBeam SEM-FIB microscope. The sample was then cut into lamellae and thinned to between 50 and 100 nm using FIB. These FIB lamellae were then visualized using a Cs-corrected STEM (ThermoFisher Scientific X-Ant-EM) at 300 kV, a beam current of 50 pA and a 20 mrad convergence angle. The atomicresolved images of the lamellae tilted to [100]-zone axes were acquired with High Angle Annular Dark Field (HAADF) detector. Image denoising was applied using custom-made python script based on pretrained neural network [16]. The original technique based on FFT filtering was developed and used to reveal the domain patterns of ordered and disordered phases. The statistical parameters and probability density function of domain size (area and equivalent diameter) distributions were calculated and plotted.

2.3. Electrode preparation and electrochemical tests

Electrode composites were prepared by mixing 90 wt. % of active material, 5 wt. % of carbon black (C45, Alfa Aesar, 99.9 %) and 5 wt. % of poly(vinylidene fluoride) (Sigma-Aldrich) in N-methyl-2-pyrrolidone (NMP, Sigma Aldrich, 99.5 %) with 30 wt. % of dry matter. The resulting slurries were dried in an oven at 80 °C overnight, then the 16 mm diameter electrodes were cut, calendared and dried at 80 °C under a dynamic vacuum overnight. The resulting mass loading of the electrodes was 6–7 mg/cm². Galvanostatic charge-discharge electrochemical cycling was performed in CR2032-type coin cells within the voltage window of 3.0 – 4.9 V ν s. Li $^+$ /Li. The Li metal was used as a counter electrode, the 1 M solution of LiPF $_6$ in ethylene carbonate and dimethyl

carbonate (EC-DMC, 1:1 vol. mixture) was used as an electrolyte, and two layers of Celgard were used as separators. The detailed electrochemical cycling protocols are described in **Table S1**.

3. Results and discussion

3.1. In situ temperature-controlled NPD of LiNi $_{0.46}$ Mn $_{1.54}$ O $_4$ and LiNi $_{0.5}$ Mn $_{1.5}$ O $_4$

To investigate the impact of the overall Mn/Ni ratio on the Mn/Ni ordering during reheating of the as-prepared LNMO samples, in situ temperature-controlled NPD experiments are reported for the globally stoichiometric $LiNi_{0.5}Mn_{1.5}O_4$ (Mn/Ni = 75/25) and Mn-rich $LiNi_{0.46}Mn_{1.54}O_4$ (Mn/Ni = 77/23) LNMO samples under an air atmosphere. Additionally, the in situ experiment was conducted under an oxygen atmosphere for LiNi_{0.46}Mn_{1.54}O₄ to investigate the impact of partial oxygen pressure (pO₂). A preparation procedure of the pristine LiNi_{0.5}Mn_{1.5}O₄ (hereafter the 75/25) and LiNi_{0.46}Mn_{1.54}O₄ (hereafter the 77/23) samples is described in Experimental section. According to SXRPD and NPD data, both 75/25 and 77/23 samples contain the disordered LNMO spinel and the impurity phases. Detailed description of the Rietveld refinement of SXRPD and NPD data of the 75/25 and 77/ 23 samples can be found in supplementary information. The Rietveld plots are presented in Figure S1. The scanning electron microscopy images of the pristine samples can be found in Figure S2.

Selected NPD patterns collected during the *in situ* experiments in the range of $600-725\,^{\circ}\text{C}$ are presented in Fig. 1. The contour plots, representing the evolution of NPD patterns during the *in situ* experiments, can be found in **Figure S3**. During heating of the 77/23 sample under an air atmosphere (77/23 Air), low-intense superstructure reflections of the

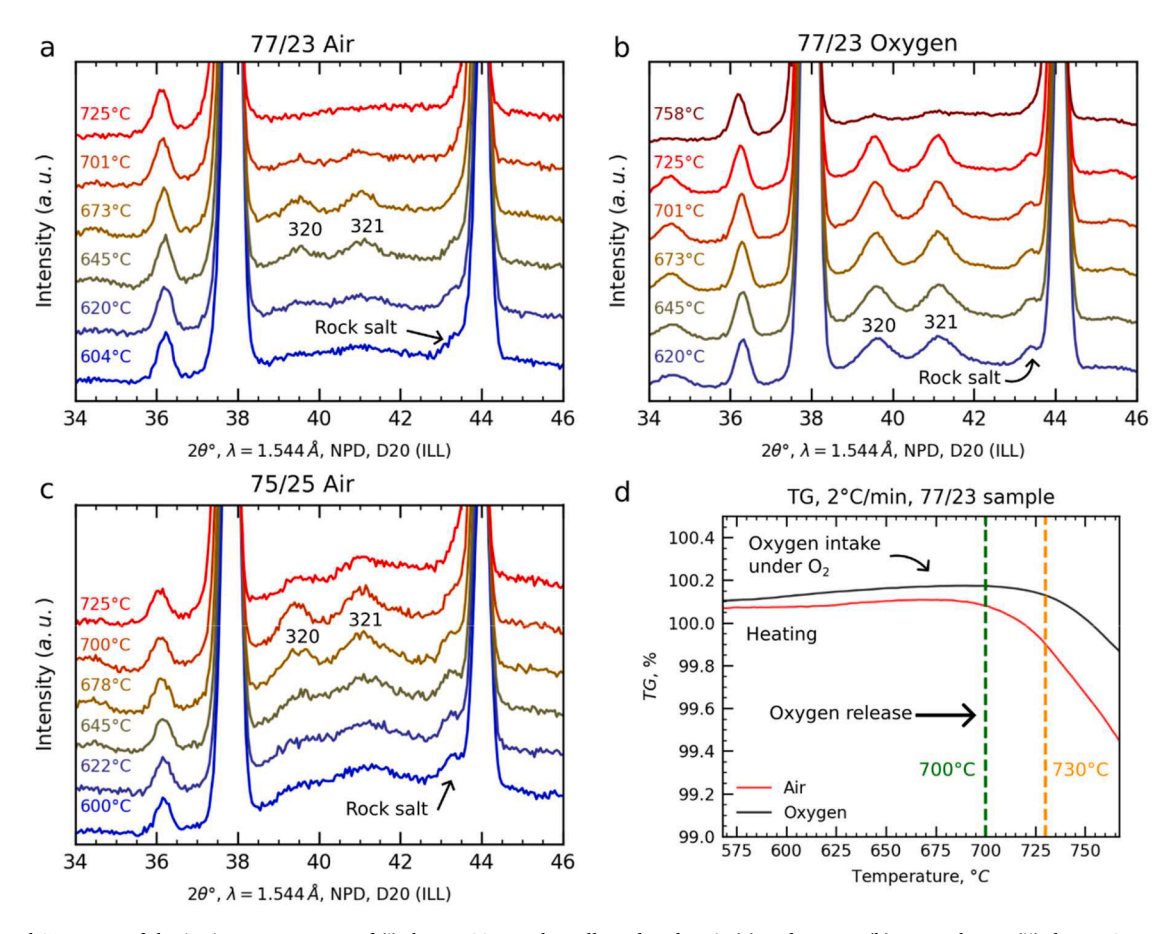


Fig. 1. Selected 2θ° range of the *in situ* NPD patterns of (i) the 77/23 sample, collected under air (a) and oxygen (b) atmospheres; (ii) the 75/25 sample, collected under air (c). Thermogravimetric (TG) curves of the 77/23 sample, collected during heating under air and oxygen atmospheres (d).

ordered LNMO phase appear at $T>600~^\circ C$ and disappear at $T\approx700~^\circ C$ (Fig. 1a and Figure S3), indicating that the Mn/Ni ordering process happens in the range of 600–700 $^\circ C$. In the case of the 77/23 sample under oxygen (77/23 Oxygen), the superstructure reflections appear at $T\approx580~^\circ C$, and they are still present till $T\approx750~^\circ C$ (Fig. 1b and Figure S3). In other words, an increase of pO_2 expands the temperature range of Mn/Ni ordering towards 580–750 $^\circ C$ in the case the 77/23 sample. Additionally, the intensities of the superstructure reflections are significantly higher for the samples treated in oxygen than for those treated in air, suggesting a greater degree of the Mn/Ni ordering under these conditions.

Similarly, when the 75/25 sample is heated under air (75/25 Air), the Mn/Ni ordering begins at T $\approx 600~^{\circ}C$ and continues till T $\approx 700~^{\circ}C$ (Fig. 1c). However, the greater intensity of the superstructure reflections in the NPD pattern of the 75/25 sample at 700 $^{\circ}C$, compared to the NPD

pattern of the 77/23 Air sample at 701 $^{\circ}$ C, suggests a higher degree of the Mn/Ni ordering in the 75/25 Air sample at this temperature.

To quantitatively analyze the structural evolution of the LNMO phases in the samples during the *in situ* experiments, a sequential Rietveld refinement was performed, for which the structural model of the ordered LNMO phase was used. Both Ni and Mn atoms were placed into the 4b and 12d octahedral sites and refined with the following constraint for each site: Ni+Mn = 100 %. The structural model can be described as $\text{Li}(\text{Ni}_{0.5\text{-}x}\text{Mn}_x)_{4b}(\text{Mn}_{1.5\text{-}y}\text{Ni}_y)_{12d}\text{O}_4$. The detailed description of the Rietveld refinement procedure can be found in **supplementary information**.

To simplify the overall discussion on the Rietveld refinement results, the introduction of an ordering parameter, δ , is proposed, which indicates how closely the distribution of Ni and Mn across the 4b and 12d sites approximates an ideal ordered distribution. The ordering

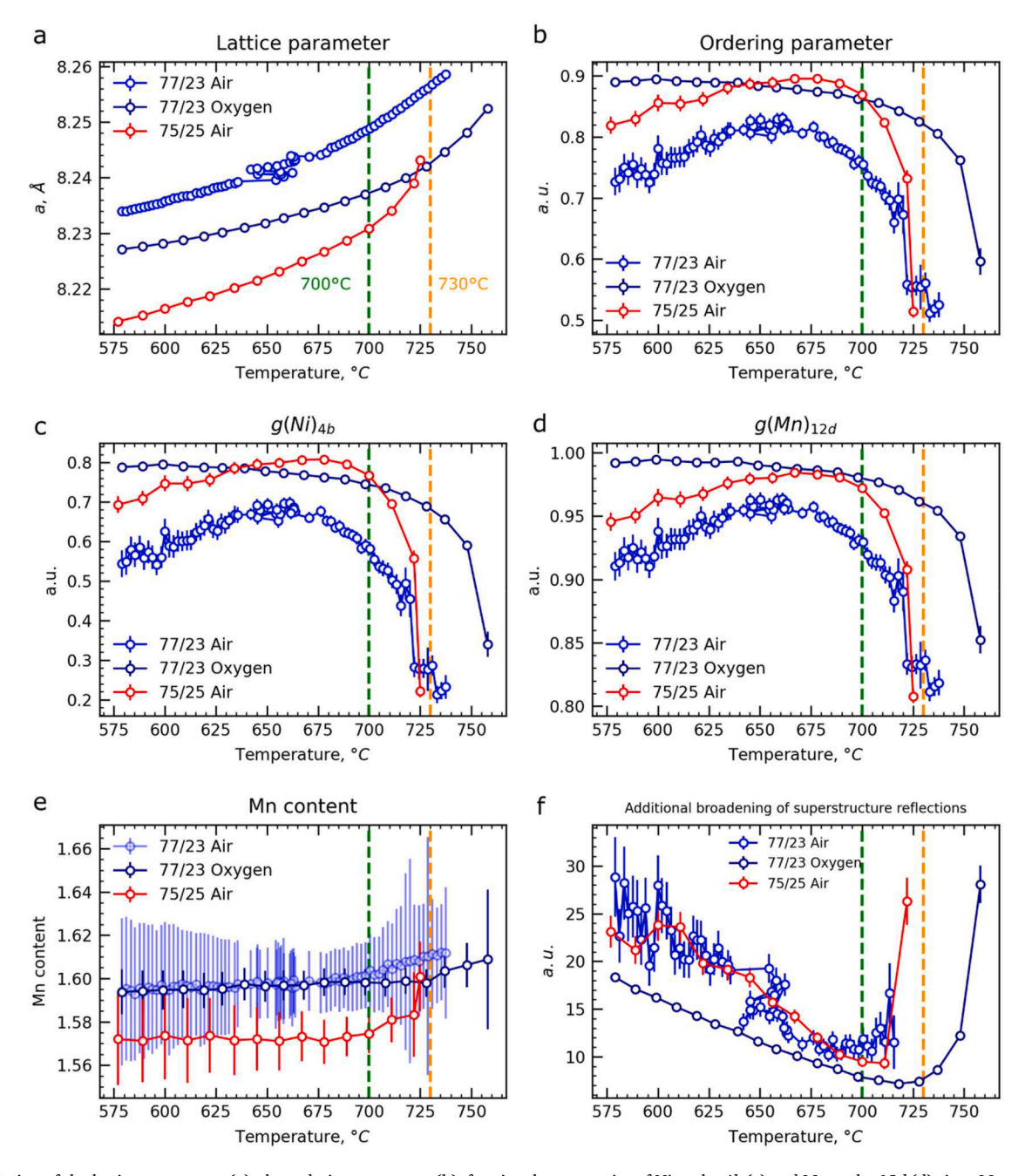


Fig. 2. Evolution of the lattice parameters (a), the ordering parameter (b), fractional occupancies of Ni at the 4*b* (c) and Mn at the 12*d* (d) sites, Mn content (e) and the additional broadening superstructure reflections (f) in the LNMO during *in situ* experiments, derived from the Rietveld refinement.

parameter δ is calculated using the following formula:

$$\delta = \frac{g(Ni)_{4b} + g(Mn)_{12d}}{2} \tag{2}$$

where $g(Ni)_{4b}$ and $g(Mn)_{12d}$ are the fractional occupancies of Ni and Mn at the 4b and the 12d sites, respectively. For the Mn/Ni = 75/25 composition, in the case of the ideal ordered distribution: $g(Ni)_{4b} = 1$, $g(Mn)_{12d} = 1$ results in $\delta = 1$. In the case of complete Mn/Ni disordering between the 4b and the 12d sites: $g(Ni)_{4b} = 0.25$, $g(Mn)_{12d} = 0.75$ resulting in $\delta = 0.5$. It is important to note that for Mn/Ni = 77/23, the ideal distribution of Ni and Mn between the 4b and the 12d sites cannot be fully achieved due to Mn excess, which results in the permanent presence of Mn at the 4b sites. For the ideally ordered LiNi $_{0.46}$ Mn $_{1.54}$ O4: $g(Ni)_{4b} = 0.92$, $g(Mn)_{12d} = 1$, leading to $\delta = 0.96$. The refined fractional occupancies of Ni and Mn at the 4b and the 12d sites, respectively, can be found in Fig. 2c-d.

Another important factor to consider is an additional broadening of the superstructure reflections of the ordered LNMO phase. It is well-known [9,10] that at the particle level, samples of the ordered LNMO consist of small ordered domains, which gives rise to additional size broadening of the superstructure reflections, coming from the ordering of Ni and Mn between the 4b and the 12d sites ($P4_332$ S.G.), compared to the reflections corresponding to the spinel framework ($Fd\overline{3}m$ S.G.). To account for this broadening of these reflections was refined, according to the work of Casas-Cabanas et al. [9]. Then, the average size of the ordered domains can be calculated, using the Scherrer equation. However, due to the inability to subtract the instrumental function from the experimental setup of the D20 diffractometer, the size of the ordered domains was not calculated. The refined values of the additional broadening of superstructure reflections can be found in Fig. 2f.

The discussion on the refinement results should begin with the importance of the value of the lattice parameter of the LNMO phase. The lattice parameter depends on composition and on the oxidation state of Mn cations in the LNMO phase. In LiNi_{0.5}Mn_{1.5}O₄, only Ni²⁺ and Mn⁴⁺ are present, whereas in the case of LiNi_{0.46}Mn_{1.54}O₄, the Mn excess results in the presence of Mn³⁺ cations for charge compensation, leading to LiNi_{0.46}Mn_{0.08}Mn_{1.46}O₄. Mn³⁺ cations possess a larger ionic radius of 0.65 Å (CN = 6), compared to 0.53 Å for Mn⁴⁺ cations (CN = 6) and therefore, the presence of Mn³⁺ cations causes an increase in the lattice parameters, which can be used for the qualitative comparison of the amount of Mn³⁺ cations (Mn content) in the LNMO phase. The refined Mn content, calculated from the occupancies of Ni and Mn at the 4b and the 12d sites can be found in Fig. 2e. However, due to relatively large error bars, the refined Mn contents of 77/23 Air and 77/23 Oxygen are statistically similar, but statistically different from that of 75/25 Air.

As shown in Fig. 2a, within the temperature range of 575-700 °C during the *in situ* experiments, the lattice parameter of the LNMO phase in the 77/23 Air sample is larger than that of the 75/25 Air sample. This difference can be attributed to the higher Mn content in the 77/23 sample. In the 77/23 Oxygen sample the lattice parameter decreases compared to that of the 77/23 Air, although remaining higher than that of the 75/25 Air. The reduction in lattice parameter for the 77/23 Oxygen, compared to the 77/23 Air, can be explained by oxygen uptake, which shifts the equilibrium towards the formation of a LNMO phase with a smaller Mn content by reducing the amount of rock salt impurity.

The observed trends in the Mn content correlate well with the evolution in the ordering parameter (Fig. 2b). The highest values of the ordering parameter are observed for the 75/25 Air and the 77/23 Oxygen samples, where the Mn content (lattice parameter) is lower compared to that of the 77/23 Air sample. The highest ordering parameter value is seen for the 75/25 Air sample at T \approx 700 °C, which has the lowest Mn content. Therefore, our results suggest that the ordering parameter – reflecting the distribution of Ni and Mn between the 4b and the 12d sites – depends on the Mn content in the LNMO phase.

Lower Mn content leads to a higher ordering parameter.

It is important to note that the sharp decline in the ordering parameters at T $\approx 690\,^{\circ}\text{C}$ for the 77/23 Air sample, at T $\approx 700\,^{\circ}\text{C}$ for the 75/25 Air sample, and at T $\approx 730\,^{\circ}\text{C}$ for the 77/23 Oxygen sample correspond well with changes in the slope of the lattice parameters as a function of temperature. These changes can be attributed to an increase in the Mn content, which is associated with the oxygen release. Thermogravimetric analysis (TG) results obtained for the 77/23 sample (Fig. 1d) indicate that oxygen release begins at T $\approx 700\,^{\circ}\text{C}$ in an air atmosphere, whereas in an oxygen atmosphere it starts at T $\approx 730\,^{\circ}\text{C}$, aligning well with the observed changes in the slope of the lattice parameters. The TG data also clearly show the oxygen intake (weight intake at T $\geq 600\,^{\circ}\text{C}$) in the case of heating of the 77/23 sample under oxygen. As discussed above, this oxygen intake decreases the Mn content in the LNMO phase.

From the above results, a clear correlation can be established between the ordering parameter and the Mn content in the LNMO phase. With higher Mn content, the ordering parameter decreases. It is interesting to compare our results with the work of Aktekin et al. [11], in which the authors conducted a similar in situ temperature-controlled NPD study (in air) of Mn-rich disordered LNMO, but with a Mn/Ni ratio of 78/22, corresponding to LiNi_{0.44}Mn_{1.56}O₄. According to their results, the disordering of Ni and Mn begins significantly earlier – at around 630 °C – and the LNMO phase becomes almost completely disordered by T \approx 700 °C. Based on these results, they concluded that it was possible to synthesize a fully disordered LNMO phase without inducing oxygen deficiency or the formation of rock salt impurities. However, it is important to note that this conclusion may only be valid for LiNi_{0.44}Mn_{1.56}O₄ (Mn/Ni = 78/22) and cannot be generalized to lower Mn/Ni ratios.

The *in situ* NPD data described above were collected during the heating of disordered LNMO samples. For the 77/23 Oxygen sample, additional NPD patterns were also collected during cooling from 800 °C at the same rate of 1 °C/min. A comparison of the diffraction patterns collected during heating and cooling is shown in **Figure S4** (top). A clear hysteresis between heating and cooling was observed, manifested as delayed Mn/Ni ordering (*i.e.*, superstructure peaks) of \sim 70 °C during cooling (**Figure S4**, top).

This hysteresis correlates well with that observed in TGA curves (**Figure S4, bottom left**). Moreover, this TGA hysteresis helps explain the observed difference in lattice parameters between heating and cooling, derived from the Rietveld refinement (**Figure S4, bottom right**): since, at any given temperature in the range of 650–775 °C, the observed weight of the sample during cooling is higher than the weight during heating, the sample is more oxygen-deficient during heating. Consequently, the Mn content in the LNMO spinel phase is higher during heating in this range of temperatures, leading to smaller lattice parameters. A similar hysteresis in lattice parameters was also reported by Wang *et al.* [8] in lab-scale *in situ* XRPD experiments with LNMO (Mn/Ni = 75/25).

One possible cause of this hysteresis is the presence of a rock-salt impurity phase. Cabana *et al.* [5] reported that rock salt impurity domains within single crystals of LNMO tend to form near the surface of crystals. These domains may hinder oxygen diffusion from the surface to bulk of the crystal, therefore delaying the Mn/Ni ordering during cooling.

In light of the observed hysteresis between heating and cooling, it is important to emphasize the critical role of cooling conditions for synthesis of LNMO. Faster cooling rates are expected to increase the extent of hysteresis, further delaying Mn/Ni ordering, increasing the amount of rock salt impurity and making it more difficult for the system to reach its thermodynamic equilibrium state.

Another notable observation is that, for the 77/23 Air sample, a slight decrease in the ordering parameter (Mn/Ni disordering) begins at T $\approx 660~^{\circ}\text{C}$. However, when the same sample is heated in oxygen, which promotes oxygen intake and reduces the Mn content in the LNMO phase,

the disordering of Ni and Mn starts only at T \approx 730 °C, which corresponds to the temperature of oxygen release. Thus, under the conditions we used, achieving a fully disordered LNMO phase with Mn/Ni = 77/23 and 75/25 without inducing the impurity phase is unlikely.

Nevertheless, it is important to note that the decrease in the ordering parameter when heating the 77/23 sample in air suggests a potential opportunity to synthesize LNMO materials with a relatively high degree of mixing between Ni and Mn at the 4b and 12d sites. This raises the question of how the size of the ordered domains changes as the ordering parameter decreases. The refined values of the additional broadening of the superstructure reflections (Fig. 2f) decrease until T \approx 700 °C for the 77/23 Air and the 75/25 Air experiments, and until T \approx 730 $^{\circ}\text{C}$ for the 77/23 Oxygen experiment. This additional broadening is inversely proportional to the size of the ordered domains, meaning that as the additional broadening decreases, the size of the ordered domains increases. In other words, despite the decrease in the ordering parameter starting at T \approx 660 $^{\circ}\text{C}$ in the 77/23 Air experiment, the size of the ordered domains continues to increase, which seems counter-intuitive. Therefore, to study this phenomenon in more details, the next section thoroughly discusses series of 77/23 and 75/25 samples prepared at different temperatures in the range of 625-725 °C in air or oxygen atmospheres.

3.2. Comprehensive structural investigation of the series of 77/23 and 77/25 samples

The series of 77/23 Air, 77/23 Oxygen, 75/25 Air, and 75/25 Oxygen samples were prepared by annealing, followed by fast cooling (5 $^{\circ}$ C/

min), the pristine 77/23 and 75/25 materials and in either air or oxygen atmospheres. The detailed synthesis procedure can be found in the Experimental section. It should be noted that fast cooling was purposely implemented to investigate Mn/Ni ordering and phase equilibrium during synthesis process in the selected temperature range. A slow cooling process would affect these parameters.

The NPD and SXRPD patterns for all 20 samples are presented in **Figure S5** and **Figure S6**. A careful analysis of the SXRPD patterns revealed that for the 77/23 Air 725 °C and 75/25 Air 725 °C samples, the main reflections of the LNMO phase are split, which is particularly noticeable at high *Q*-range (**Figure S5**). Therefore, the subsequent discussion of the structural analysis results is divided into the following subsections. The first subsection addresses the correlation between the Mn content and the ordering parameter in samples where no reflection splitting is observed. The second subsection focuses on studying Mn/Ni ordering at the particle level using HR-STEM for the samples of the 77/23 Air series. The final subsection will explore the detailed reasons behind the reflection splitting observed in the 77/23 Air 725 °C and 75/25 Air 725 °C samples.

3.3. Correlation between the mn content and the ordering parameter in the LNMO spinel phase

For the combined Rietveld refinement of the SXRPD and NPD patterns of the samples without the reflection splitting, the same structural model $\text{Li}(\text{Ni}_{0.5\text{-x}}\text{Mn}_x)_{4b}(\text{Mn}_{1.5\text{-y}}\text{Ni}_y)_{12d}\text{O}_4$ of ordered LNMO was used for the Rietveld refinements, as for the analysis of the in situ experiments. The detailed description of the Rietveld refinement procedure can be

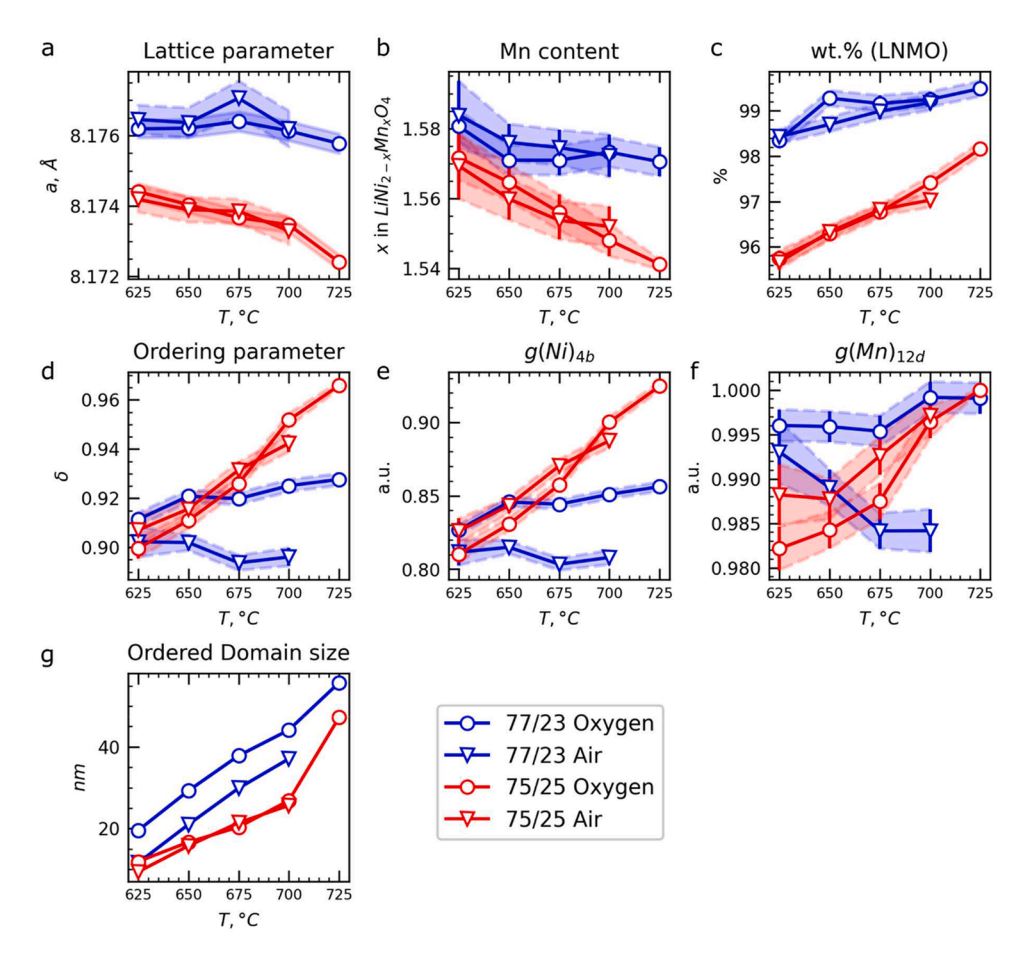


Fig. 3. Results of the combined Rietveld refinement of SXRPD and NPD patterns of the series of LNMO samples. The evolution of: lattice parameters (a), Mn content (b), weight fraction (c), the ordering parameter (d), the fractional occupancies of Ni at the 4b (e) and Mn at the 12d (f) sites, and size of the ordered domains (g) in the LNMO spinel phase.

found in **supplementary information**. The refined fractional occupancies can be found in Fig. 3e-f. The experimental points, calculated and difference profiles can be found in **Figures S7-S8**.

From the Rietveld refinement results (Fig. 3), it is evident that all samples from the 75/25 Air and 75/25 Oxygen series have smaller lattice parameters for the LNMO spinel phase (Fig. 3a) compared to the 77/23 Air and 77/23 Oxygen series. As noted earlier, lattice parameters are highly sensitive to the Mn content in the LNMO spinel phase. Indeed, it is as expected found lower for the 75/25 Air and 75/25 Oxygen samples than for the 77/23 Air and 77/23 Oxygen samples (Fig. 3b).

A significant difference is also observed in the weight fraction of the LNMO spinel phase (Fig. 3c), with notably lower values in the 75/25 Air and 75/25 Oxygen samples compared to the 77/23 Air and 77/23 Oxygen samples. These results are in good agreement with our previous work [13], where it was noted that a global excess of Mn in the samples increased the structural stability of the LNMO spinel phase.

It is also worth noting that samples prepared from the same pristine sample and at the same temperatures, but in different atmospheres, have statistically identical values for the lattice parameters (Fig. 3a), the Mn content (Fig. 3b), and the weight fraction of the LNMO spinel phase (Fig. 3c). For each series of samples, increasing the annealing temperature in the 625–725 °C range leads to a slight decrease in the lattice parameters and Mn content in the LNMO spinel phase, along with a slight increase in the weight fraction of the LNMO spinel phase in the samples.

In the case of the 77/23 Air and 77/23 Oxygen series, the size of the ordered domains (Fig. 3 g) is larger than in the 75/25 Air and 75/25 Oxygen series, which is somewhat unexpected. The Mn/Ni ratio of 75/25 (3/1) corresponds to the ideal ratio between the 4b and the 12d sites in the crystal structure of the ordered LNMO spinel phase. It can be hypothesized that the higher weight fraction of the LNMO spinel phase in the 77/23 samples promotes greater growth of the ordered domains. Interestingly, annealing in an oxygen atmosphere does not affect the domain size for the 75/25 series, whereas in the 77/23 series, the size of the ordered domains increases after oxygen annealing. For the 75/25 Air and 75/25 Oxygen series, annealing in oxygen also does not impact the ordering parameter (Fig. 3d); in both series, the ordering parameter increases with higher annealing temperatures.

In contrast, for the two 77/23 series, annealing under oxygen significantly alters the behavior of the ordering parameter. In the 77/23 Air series, the ordering parameter slightly decreases with increasing annealing temperature, while in the 77/23 Oxygen series, the ordering parameter is higher and increases as the temperature rises. At the same time, the size of the ordered domains in both series continues to grow with increasing temperature. In other words, in the 77/23 Air series, the two parameters related to Mn/Ni ordering change in opposite directions.

At first glance, the reason for the different behavior of the ordering parameter in the 77/23 Air and 77/23 Oxygen series is not obvious, since all other structural parameters - lattice parameter, Mn content, and the weight fraction of the LNMO spinel phase - are statistically similar in these samples. However, it can be speculated that oxygen intake is more pronounced during annealing in an oxygen atmosphere, which reduces the amount of impurity phases and Mn³⁺ cations in the LNMO spinel phase, leading to the increase of the ordering parameter. In contrast, during annealing in air, oxygen uptake is minimal, meaning that the Mn content in the LNMO spinel phase remains unchanged, and thus, the ordering parameter is unaffected. Yet, the difference in these parameters is so slight that it cannot be detected. This hypothesis is partially supported by the TG data. It was previously shown that when the pristine 77/23 sample was heated in an oxygen atmosphere, the weight gain, corresponding to oxygen intake, was higher than in the case of heating in air (Fig. 1f).

The results described above, along with the *in situ* NPD experiments, show a direct correlation between the Mn content in the LNMO phase and the ordering parameter. As the Mn content in the LNMO spinel phase increases, the ordering parameter decreases. This is particularly

obvious when comparing the changes in Mn content in the LNMO spinel phase of the 75/25 and 77/23 series (Fig. 3b) with the changes in the ordering parameter (Fig. 3d). Starting at 675 °C, the Mn content in the LNMO spinel phase of the 75/25 samples is lower than that of the 77/23 samples. Similarly, from 675 °C onwards, the ordering parameter in the 75/25 samples is higher than in the 77/23 samples.

3.4. Presence and distribution of the ordered domains at the particle level

To investigate Mn/Ni ordering at the particle level, we developed a novel approach using HR-STEM and FFT filtering to visualize Mn/Ni ordering. The samples selected for this analysis were 77/23 Air 625 °C, 77/23 Air 650 °C, 77/23 Air 675 °C, and 77/23 Air 700 °C. Atomicallyresolved HAADF-STEM images were acquired along the [100] direction of the lamellae (details on lamellae preparation can be found in the Experimental section). The [100] direction was chosen because it clearly displays Mn/Ni ordering within the LNMO crystal structure (Figure S9). The collected images were then processed with fast Fourier transform (FFT) analysis, where FFT filtering was applied to the HAADF-STEM images using a circular mask centered exclusively on the superstructure reflections of the ordered LNMO spinel phase. Following the inverse FFT transformation, the images showed variations in intensity contrast corresponding to Mn/Ni ordered and disordered areas: high-intensity regions indicated ordered areas, while low-intensity regions represented disordered areas. A schematic outline of this methodology is provided in Figure S9.

The process of image segmentation was employed to extract the geometric characteristics of the domains. It is important to note that segmentation of the FFT-filtered HR-HAADF-STEM images was performed manually – the boundaries of the ordered domains were traced by hand. This approach was chosen because automatic segmentation methods failed, likely due to complex contrast variations in the images. We acknowledge that manual segmentation may introduce a degree of subjectivity. However, to minimize this effect, hundreds of images were acquired and analyzed for each sample.

After the segmentation process, the equivalent diameters were plotted as a function of both the distance from the surface of the particle and the annealing temperature. It is worth noting that the theoretical resolution depth for atomic-resolution STEM imaging at an acceleration voltage of 300 keV and an angular aperture of 20 mrad, using an electron microscope equipped with a correction for spherical aberrations, has been estimated to be approximately 10 nanometers [17]. This finding allows us to conclude that ordered and disordered areas have been mapped on the surface and in the subsurface layer of the lamella.

This approach allowed us to visualize Mn/Ni ordering at the single-particle level. For clarity in the following discussion, HAADF-STEM images combined with inverse FFT images for the 77/23 Air 700 °C sample are shown in Fig. 4. These images reveal the formation of ordered domains with irregular shapes that are homogeneously distributed throughout each particle (Fig. 4a). The ordered domains are separated by disordered regions. Furthermore, the size of these ordered domains does not depend on the distance from the particle surface (Fig. 4c). Additionally, the analysis of the domain size distribution shows that the average size of the ordered domains increases with annealing temperature (Fig. 4d-f). It is worth noting that the domain sizes obtained from HR-STEM correlate well with those derived from the Rietveld refinement of NPD patterns, confirming the validity of the structural model used in the Rietveld refinements.

It should be noted that in our HR-STEM study, we did not specifically focus on evaluating the potential influence of electron beam exposure and lamella preparation on the distribution of ordered domains. So, the future HR-STEM research on LNMO materials could benefit from a more detailed assessment of beam and preparation effects on the domain structure. In our experiments, only a single image was taken per spot to minimize possible beam damage and alteration of the ordered domain structure. Nonetheless, these factors may have some effect, the excellent

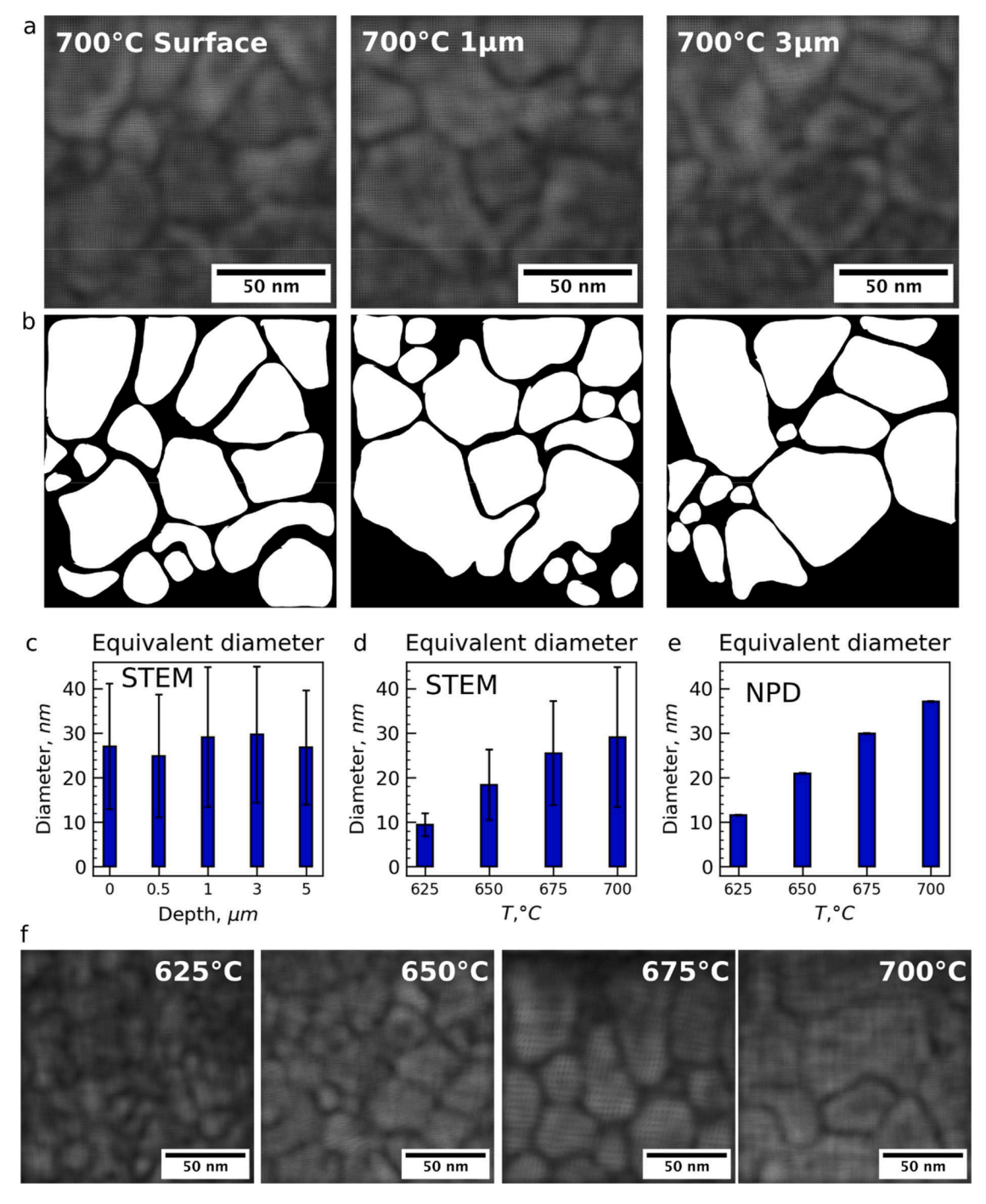


Fig. 4. Selected FFT-filtered HR-HAADF-STEM images at varying depths from the lamella edge (surface, 1 μ m, and 3 μ m) for the 77/23 Air 700 °C sample (a). Binarized representations of the images in (a), showing ordered domains (white) and disordered regions (black) (b). Evolution of ordered domain size with particle depth (c) for the 77/23 Air 700 °C sample, and with annealing temperature extracted from HR-HAADF-STEM (d) and NPD (e) data. FFT-filtered HR-HAADF-STEM images (acquired at 5 μ m from the lamella edge) demonstrating evolution of domain structure in the 77/23 Air samples with annealing temperature (f).

agreement between HR-STEM (potentially destructive technique) and NPD (fully non-destructive method) supports the reliability and robustness of our observations.

The observed Mn/Ni ordering at the particle level aligns well with the hypothesis proposed by Casas-Cabanas et al. [9], who suggested two possible mechanisms for the formation of nano-sized ordered domains at the particle level: (i) formation of ordered domains within a disordered matrix (Fig. 5, top), and (ii) formation of ordered domains separated by antiphase boundaries within a globally ordered matrix (Fig. 5, bottom). Our results indicate an intermediate scenario: ordered domains are

separated by disordered regions, although the thickness (\approx 3–5 nm) of these regions is significantly smaller than the ordered domain size.

It is interesting to discuss potential reasons for the observed Mn/Ni ordering at the particle level. Since a higher Mn content in the LNMO spinel phase promotes Mn/Ni disordering, it can be assumed that the Mn/Ni ratio in the ordered domains is lower than in the disordered regions separating these domains. Given that in the ideal crystal structure of ordered LNMO, Mn/Ni = 3, we hypothesize that the ordered domains possess Mn/Ni = 3, with the overall Mn excess balanced by the presence of disordered regions, where Mn/Ni > 3. For instance, assuming a global

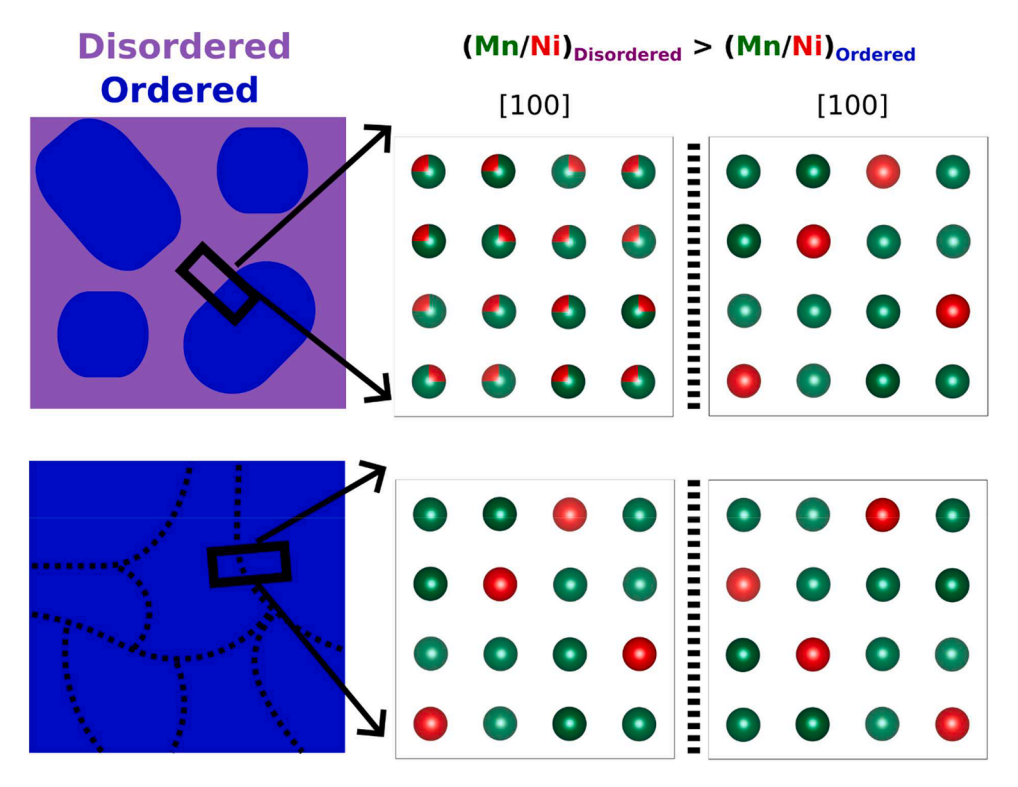


Fig. 5. Schematic representation of the possible mechanisms of the distribution of the ordered domains at the particle level: ordered domains in the disordered matrix (top), ordered domains, separated by the antiphase boundaries (dotted line), in the globally ordered matrix (bottom). The Li and O atoms in the crystal structures are not shown for simplicity. Reproduced with permission from Casas-Cabanas *et al.* [9]. (One column figure).

Mn/Ni ratio of 77/23 in the LNMO spinel phase, the following equation would describe the distribution of ordered and disordered areas:

$$LiNi_{0.46}Mn_{1.54}O_4 = pLiNi_{0.5}Mn_{1.5}O_4 + qLiNi_{0.5-x}Mn_{1.5+x}O_4$$
Ordered
Disordered
Ordered
(3)

Using material balance (stoichiometry), we can express the system with the following parametric equations:

$$p = \frac{x - 0.04}{x}, \ q = \frac{0.04}{x}, \frac{p}{q} = \frac{x - 0.04}{0.04}$$
 (4)

where the parameter x represents the chemical composition of the disordered LNMO. As shown in Eq. (4), for physically valid solutions, x must be greater than 0.04. The ratio p/q indicates the molar ratio of the ordered to disordered LNMO. Additionally, due to similar chemical compositions of the two phases, p/q also reflects their mass and volume ratios. For illustration, if we substitute x=0.08 in Eq. (4), then p/q=1 which implies that if the disordered regions have a composition of $\text{LiNi}_{0.42}\text{Mn}_{1.58}\text{O}_4$, and the ordered domains a composition of $\text{LiNi}_{0.5}\text{Mn}_{1.5}\text{O}_4$, then the mass and volume ratio between ordered and disordered regions equals roughly to one. However, HR-STEM data indicate that ordered domains are uniformly distributed throughout the lamellae and occupy a significantly larger area than the disordered areas.

From Eq. (4), we can see that increasing the Mn content in the disordered phase (increasing x) increases the quantity of the ordered phase. For example, if p/q=5, then x=0.24, corresponding to a composition of LiNi_{0.26}Mn_{1.74}O₄ in the disordered areas, or Mn/Ni \approx 6.69. Such an inhomogeneous Mn and Ni distribution between the ordered domains and disordered regions is unlikely, as it would generate substantial strains in the sample, affecting the peak shape of reflections associated with the spinel framework. Given this, we suggest that the Mn/Ni ratio in the ordered domains is also greater than 3, though lower than in the disordered regions (Fig. 5, top).

3.5. Coexistence of the ordered and disordered LNMO spinel phases

As mentioned earlier, the SXRPD patterns of the 77/23 Air 725 °C and 75/25 Air 725 °C samples revealed a splitting of diffraction reflections, which is clearly visible at high 20 angles (**Figure S5**). SXRPD measurements on the BL04 MSPD beamline, using a setup with higher angular resolution and a shorter wavelength, improved the resolution to the point where the splitting of the (311) reflection of the LNMO spinel phase could be observed (Fig. 6). The splitting of all reflections in the SXRPD patterns can be explained by the coexistence of two LNMO spinel phases in the samples.

Indexing of the SXRPD patterns using two phases with the $Fd\overline{3}m$ S.G. shows that in both samples, the lattice parameters of one phase are significantly larger than those of the other phase (Fig. 6, inset). Meanwhile, the NPD patterns of these samples display the superstructure reflections of the ordered LNMO spinel phase (Figure S10). Therefore, the LNMO spinel phases with smaller lattice parameters were identified as ordered LNMO spinel phases, while the LNMO spinel phases with larger lattice parameters were assigned as disordered LNMO spinel phases. This assumption was made because the larger lattice parameter indicates a significantly higher Mn content in the LNMO spinel phase. As shown earlier, higher Mn content in the LNMO spinel phase leads to the disordering of Mn and Ni. It is worth noting that the reflection splitting on the NPD patterns is less pronounced due to the lower angular resolution, but in the 77/23 Air 725 $^{\circ}$ C sample, splitting can be observed at high 2θ angles for reflections corresponding to the $Fd\overline{3}m$ S.G. (Figure \$10). Splitting of the superstructure reflections, which corresponds to the P4332 S.G., is not observed. However, it should be mentioned that the superstructure reflections exhibit additional broadening due to the small size of the ordered domains.

For the disordered LNMO spinel phase the structural model Li(Ni_{0.5-x}Mn_{1.5+x})_{16d}O₄ was used, while the structural model Li(Ni_{0.5-x}Mn_x)_{4b}(Mn_{1.5+y}Ni_y)_{12d}O₄ was implemented for the ordered LNMO spinel phase. The additional size broadening of the superstructure

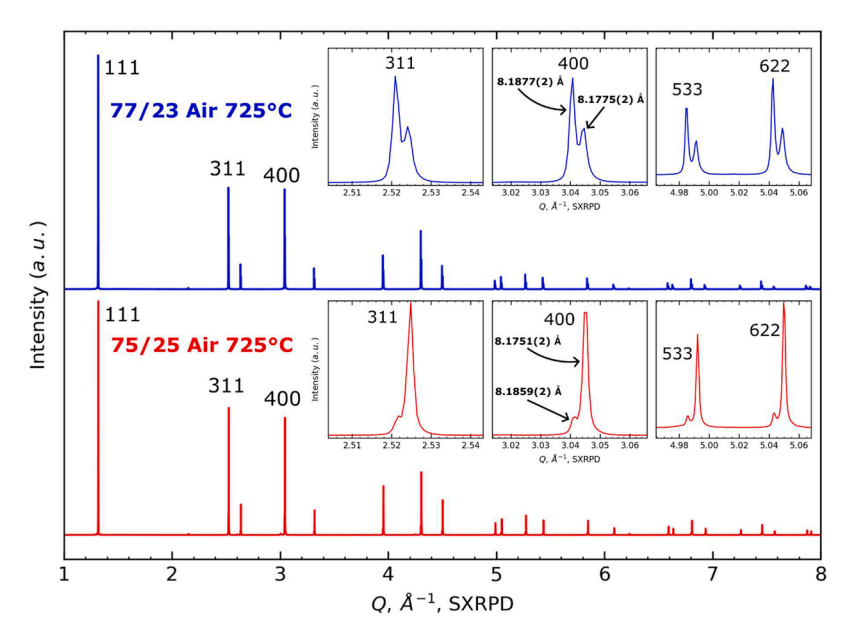


Fig. 6. SXRPD patterns of the 77/23 Air 725 °C and 75/25 Air 725 °C samples (inset: Q ranges are selected to highlight the presence of two LNMO spinel phases).

reflections of the ordered LNMO phase was refined. The results after the Rietveld refinement can be found in Table 1. The experimental points, calculated and difference plots can be found in Figure S11.

As shown in Table 1, the 77/23 Air 725 °C sample contains a greater amount of the disordered phase compared to the 75/25 Air 725 °C sample. The chemical composition of the ordered and disordered LNMO spinel phases in these samples is identical within the margin of refinement error. Surprisingly, the size of the ordered domains in the 77/23 Air 725 °C sample is significantly larger than in the 75/25 Air 725 °C sample. We do not have a definitive answer for this result, but we can hypothesize that the presence of a greater amount of the rock salt impurity in the 75/25 Air 725 °C sample, compared to the 77/23 Air 725 °C sample, might limit the growth of the ordered domains. In the case of the combined Rietveld refinement for 77/23 Air 725 °C, the rock salt impurity phase was not included, as the statistics were insufficient to resolve its reflections.

The simultaneous presence of both ordered and disordered LNMO spinel phases can be explained by the following hypothesis. At the annealing temperature of 725 °C in an air atmosphere, the oxygen release is already occurring, leading to the formation of the impurity phase, the reduction of $\rm Mn^{4+}$ to $\rm Mn^{3+}$ cations, and the transformation of the ordered LNMO spinel phase into the disordered one. However, at this temperature, the amount of oxygen lost is relatively small (Fig. 1d). It can thus be assumed that the oxygen loss primarily takes place in the surface regions of the particles, and with such a small amount of oxygen loss, the bulk of the particles remains unaffected. This creates compositional inhomogeneity due to the enrichment of the surface regions with $\rm Mn^{3+}$ cations and the impurity phase, which facilitates the formation of

 $\label{thm:combined} \begin{tabular}{ll} \textbf{Table 1} \\ \textbf{Results after the combined Rietveld refinement of the SXRPD and NPD patterns} \\ \textbf{of the 77/23 Air 725 °C and 75/25 Air 725 °C samples.} \\ \end{tabular}$

Sample ID	Ordered/ Disordered, wt. %	Mn/Ni, Ordered	Mn/Ni, Disordered	Ordered domain size, nm
77/23 Air 725 °C	45.3/54.7(2)	1.54/0.46 (2)	1.58/0.42(1)	83
75/25 Air 725 °C	88.4/8.9(1) ¹	1.541/ 0.459(3)	1.60/0.40(1)	38

 $^{^1}$ In the 75/25 Air 725 $^{\circ}\text{C}$ the rock salt impurity phase is also present with wt. % of 2.7(1).

the disordered LNMO spinel phase in these regions. To test this hypothesis, selected-area electron diffraction of these samples could provide valuable insights.

In conclusion to this section, our comprehensive structural investigation of the series of samples with different Mn/Ni ratios (75/25 and 77/23), prepared in the temperature range of 625–725 $^{\circ}$ C under both air and oxygen atmospheres, revealed that the degree of ordering between Mn and Ni at the 4b and 12d sites (the ordering parameter) directly correlates with the Mn content in the LNMO spinel phase: the higher the Mn content, the lower the ordering parameter.

Our results also show that as the annealing temperature increases, the size of the ordered domains grows in all series. For the 77/23 Oxygen, 75/25 Air, and 75/25 Oxygen series, the ordering parameter also increases with higher annealing temperatures. However, in the 77/23 Air series, the ordering parameter decreases with increasing temperature. Due to this unusual behavior of the ordering parameter, studying the electrochemical properties of the 77/23 Air and 77/23 Oxygen samples becomes a highly intriguing task. Additionally, in the 77/23 Air 725 °C and 75/25 Air 725 °C samples, we observed the coexistence of both ordered and disordered LNMO spinel phases, which, to the best of our knowledge, has never been reported in the literature. In the next section, the electrochemical properties of the 75/25 and 77/23 series will be thoroughly discussed.

3.6. Electrochemical study

The detailed electrochemical cycling program can be found in **Table S1**. The galvanostatic charge-discharge curves collected at 0.1C-0.1D rates during the 1st cycle for the 4 series of samples (i.e. 20 samples) can be found in Fig. 7. It can be seen that the 77/23 Air and 75/25 Air samples demonstrate higher discharge capacities in the first cycle compared to the samples from the 77/23 Oxygen and 75/25 Oxygen series. The difference is especially pronounced between the 75/25 Air and 75/25 Oxygen series. In one of our previous studies [13], we showed that materials with a higher Mn content in the LNMO spinel phase exhibit higher discharge capacities. As suggested in the previous section, during annealing in an oxygen atmosphere the Mn content in the LNMO spinel phase is lowered compared to the samples prepared under air. This reduced Mn content is also reflected by the smaller contribution of the redox process at \approx 4.0 V, corresponding to the Mn⁴⁺/Mn³⁺ redox couple (Fig. 7, inset). It is also worth noting that within the same series

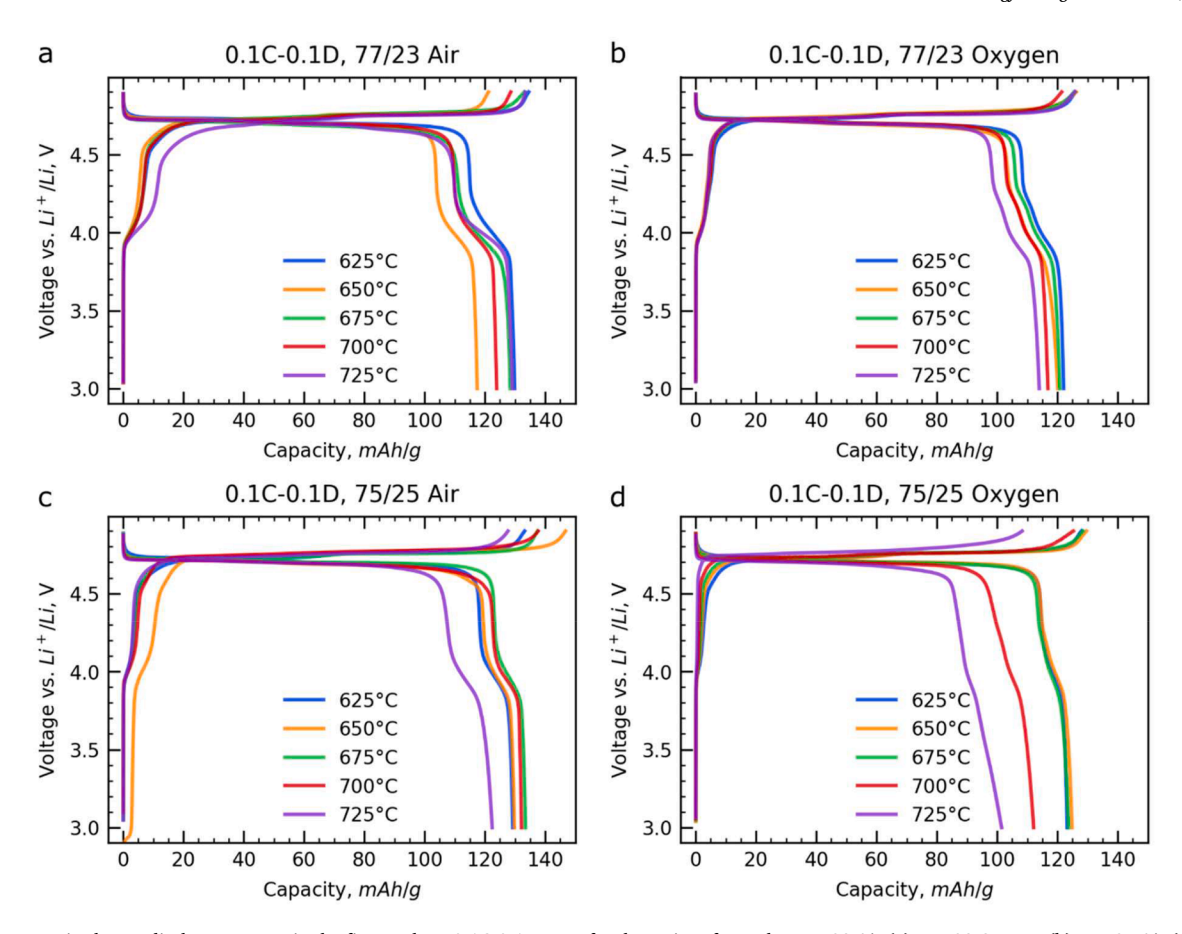


Fig. 7. Galvanostatic charge-discharge curves in the first cycle at 0.1C-0.1D rates for the series of samples: 77/23 Air (a), 77/23 Oxygen (b), 75/25 Air (c) and 75/25 Oxygen (d).

of samples (with the exception of 77/23 Air 725 $^{\circ}C$ sample), the shape of the voltage-composition profiles and the capacity gained at ≈ 4.0 V are nearly identical across the series. However, when comparing the charge-discharge curves of the air-annealed samples with those of the oxygen-annealed ones, an additional process at ≈ 4.2 V is observed in the samples prepared under oxygen.

3.7. Impact of the ordering parameter on the Mn^{4+}/Mn^{3+} redox process

A comparison of the structural data and dQ/dV curves suggests that this additional process is related to higher degrees of Mn and Ni ordering between the 4b and 12d sites. This is well illustrated in the case of the 77/23 Air and 77/23 Oxygen series (Fig. 8a). As shown earlier, samples from these series, annealed at the same temperature but under different atmospheres, have identical structural parameters except for the size of the ordered domains and the ordering parameter. It can be seen that the appearance of this additional process correlates with the higher ordering parameter values in the 77/23 Oxygen samples. Based on our data, it can thus be inferred that the occurrence of the additional process at $\approx 4.2 \text{ V}$ is associated with annealing in an oxygen atmosphere but we would like to emphasize that this process is directly linked to the degree of Mn/Ni ordering between the 4b and 12d sites, rather than being exclusively caused by oxygen annealing. For instance, in one of our previous studies [13], the charge-discharge curve of an LNMO sample with Mn/Ni = 77/23, annealed in air at 725 $^{\circ}\text{C},$ also exhibited this additional process. According to NPD data, the ordering parameter for this sample was 0.949(1), which aligns perfectly with the results described above.

It can also be speculated that the larger size of the ordered domains in the 77/23 Oxygen samples could contribute to the appearance of this additional process. However, when comparing the dQ/dV data of the

 $75/25~\rm Air~700~^{\circ}C$ and $75/25~\rm Oxygen~700~^{\circ}C$ samples (Fig. 8b), it is clear that this process is also present for the latter. According to the Rietveld refinement data, these samples have identical ordered domain sizes, but the $75/25~\rm Oxygen~700~^{\circ}C$ sample has a slightly higher ordering parameter. Thus, we can suggest that the appearance of this process is primarily due to the higher values of the ordering parameter.

For sake of clarity, we have referred to the process at $\approx 4.2~V$ as the "additional" one which, like the one occurring at $\approx 4.0~V$, is associated with the oxidation of Mn $^{3+}$ cations to Mn $^{4+}$. This is well illustrated by the 75/25 Oxygen 700 °C sample, which has lower Mn content in the LNMO spinel phase compared to the 77/23 samples. As a result, the intensity of these processes on the dQ/dV curve (Fig. 8b) is significantly lower than in the 77/23 Oxygen 700 °C sample (Fig. 8a).

It is worth noting that this additional process was also reported by Aktekin et al. [11], Kunduraci et al. [4] and Song *et al.* [18] for Mn-rich ordered LNMO samples. In studies [9] and [17], NPD was not used to assess the degree of Mn/Ni ordering in the LNMO spinel structure. In the work by Aktekin et al. [8], the LNMO sample was indeed examined by NPD; however, their structural model did not account for the additional size broadening of the superstructure reflections, which prevents a direct comparison with our results.

It is interesting to discuss the possible reasons behind the appearance of this additional process related to the $\rm Mn^{4+}/\rm Mn^{3+}$ redox couple. The most probable explanation lies within the crystal structure of the ordered domains. At higher ordering parameter values, the 12d site (Mn site) is almost completely occupied by Mn, with $\rm g(Mn)_{12d}=0.998(2)$ for the 77/23 Oxygen 700 °C sample (Fig. 3f). When there is an excess of Mn, represented as x in $\rm LiNi_{0.5-x}Mn_{1.5+x}O_4$, the crystal structure contains 2x of $\rm Mn^{3+}$ cations: $\rm LiNi_{0.5-x}^2Mn_{1.5-x}^3Mn_{1.5-x}^{4+}O_4$. Since the $\rm 12d$ site is fully occupied by Mn, and all the excess Mn resides at the $\rm 4b$ sites, it can be

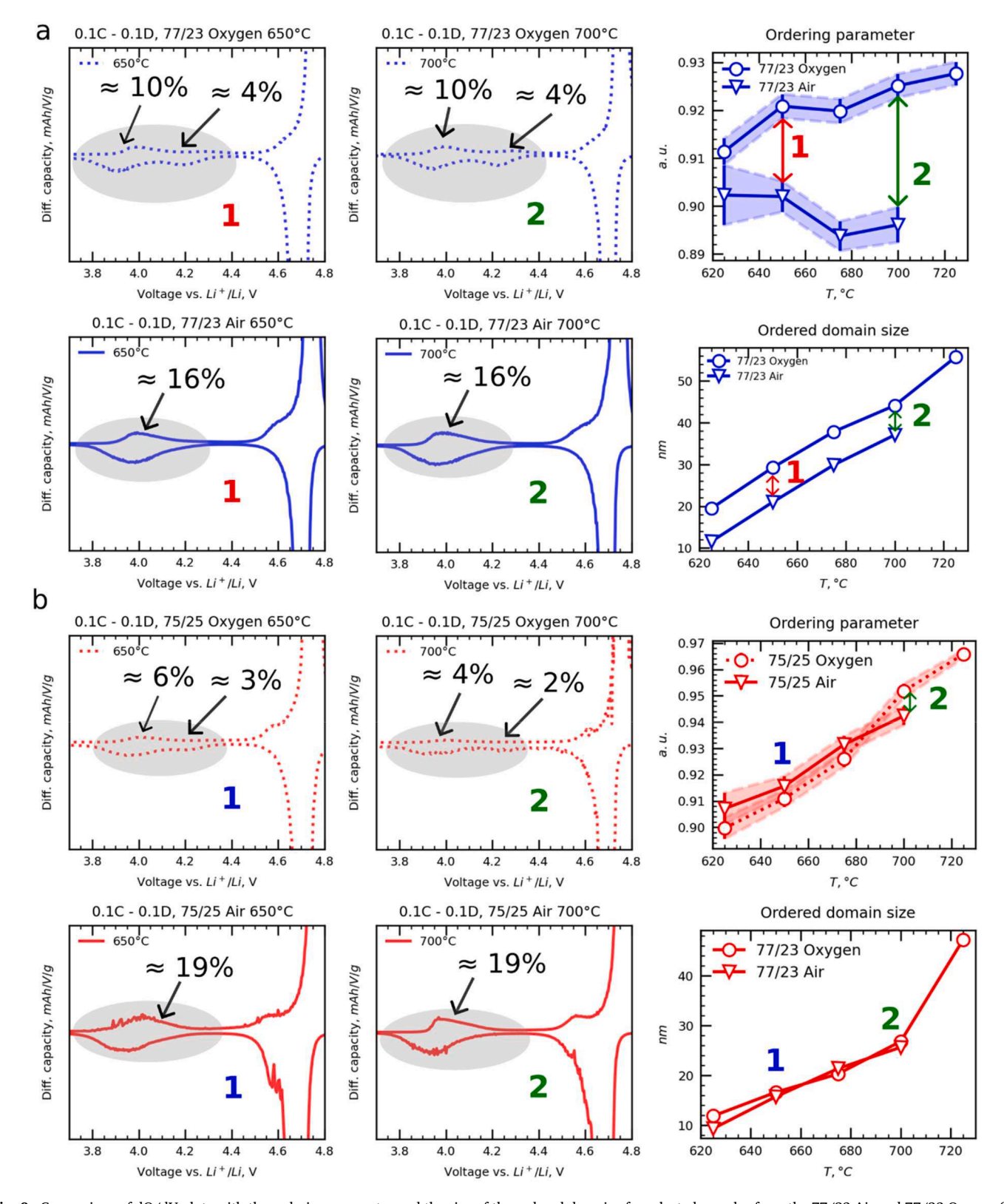


Fig. 8. Comparison of dQ/dV plots with the ordering parameter and the size of the ordered domains for selected samples from the 77/23 Air and 77/23 Oxygen (a) and for the 75/25 Air and 75/25 Oxygen (b) series. Inset: fractions of gained discharge capacities of the processes, corresponding to Mn^{4+}/Mn^{3+} redox couple.

assumed that an equal number of $\mathrm{Mn^{3+}}$ cations are present in both the 4b and 12d positions. For example, for $\mathrm{x}=0.04$, the composition would be $\mathrm{Li}\left[\mathrm{Ni_{0.46}^{2+}Mn_{0.04}^{3+}}\right]_{4b}\left[\mathrm{Mn_{0.04}^{3+}Mn_{1.46}^{4+}}\right]_{12d}\mathrm{O_4}$. This distribution implies the presence of only two types of $\mathrm{Mn^{3+}}$ cations in the crystal structure. In contrast, with greater $\mathrm{Mn/Ni}$ mixing (lower ordering parameter), $\mathrm{Ni^{2+}}$

cations would also occupy the 12d sites, increasing the number of possible configurations for ${\rm Mn}^{3+}$ distribution between the 4b and 12d sites.

In the case of $\mathrm{Li}[\mathrm{Ni}_{0.46}^{2+}\mathrm{Mn}_{0.04}^{3+}]_{4b}[\mathrm{Mn}_{0.04}^{3+}\mathrm{Mn}_{1.46}^{4+}]_{12d}\mathrm{O}_4$, the oxidation of Mn^{3+} cations in the 4b and 12d positions could occur at different

voltages. Based on an analysis of interatomic distances, it can be hypothesized that $\mathrm{Mn^{3+}}$ in the 4b sites oxidizes at higher voltages, as the M-O distances in the 4b site are larger than in the 12d site. For instance, in the 77/23 Oxygen $700\,^{\circ}\mathrm{C}$ sample, $\mathrm{d}(\mathrm{M-O})_{4b} = 2.063(1)\,\mathrm{\mathring{A}}$, while $\mathrm{d}(\mathrm{M-O})_{12d} = 1.909(2)\,\mathrm{\mathring{A}}$. Longer interatomic distances correspond to more ionic M-O bonds. It is known that with increased bond ionicity, the oxidation of transition metal cations occurs at higher voltages. However, it is important to note that the interatomic distances obtained from the Rietveld refinement are average values, and the actual distances for $\mathrm{Mn^{3+}}$ cations in these sites could differ locally.

It is also worth noting that if the scenario described just above holds true, the capacity contributions from the oxidation of both Mn^{3+} cations should be equal. However, in practice, the contribution to the total capacity from the process at ≈ 4.0 V is slightly higher than that of the process at ≈ 4.2 V (Fig. 8a). It is possible that, in reality, a small fraction of Mn^{4+} also occupies the 4b site, which would increase the amount of Mn^{3+} at the 12d sites. Additionally, it is possible that this slight extra

capacity observed at $\approx 4.0~V$ is related to Mn^{3+} cations located in the disordered regions, which are not accounted for in the structural model used for the Rietveld refinement. Nevertheless, based on the HR-STEM data presented above, Mn/Ni-ordered domains at the particle level are separated by thin disordered regions, and Mn^{3+} cations from these regions could contribute modestly to the process at $\approx 4.0~V.$

3.8. Impact of the coexistence of the ordered and disordered LNMO phases

As previously mentioned, the charge-discharge curve of the 77/23 Air 725 °C sample differs from the curves of other samples belonging to the 77/23 Air series. In this sample, both the disordered and ordered LNMO spinel phases are present. On the dQ/dV curve (Fig. 9a), three processes are clearly observed in the voltage range corresponding to the Ni⁴⁺/Ni³⁺/Ni²⁺ redox couples, whereas only two processes are typically reported for LNMO in this voltage range [1]. Notably, the third process is

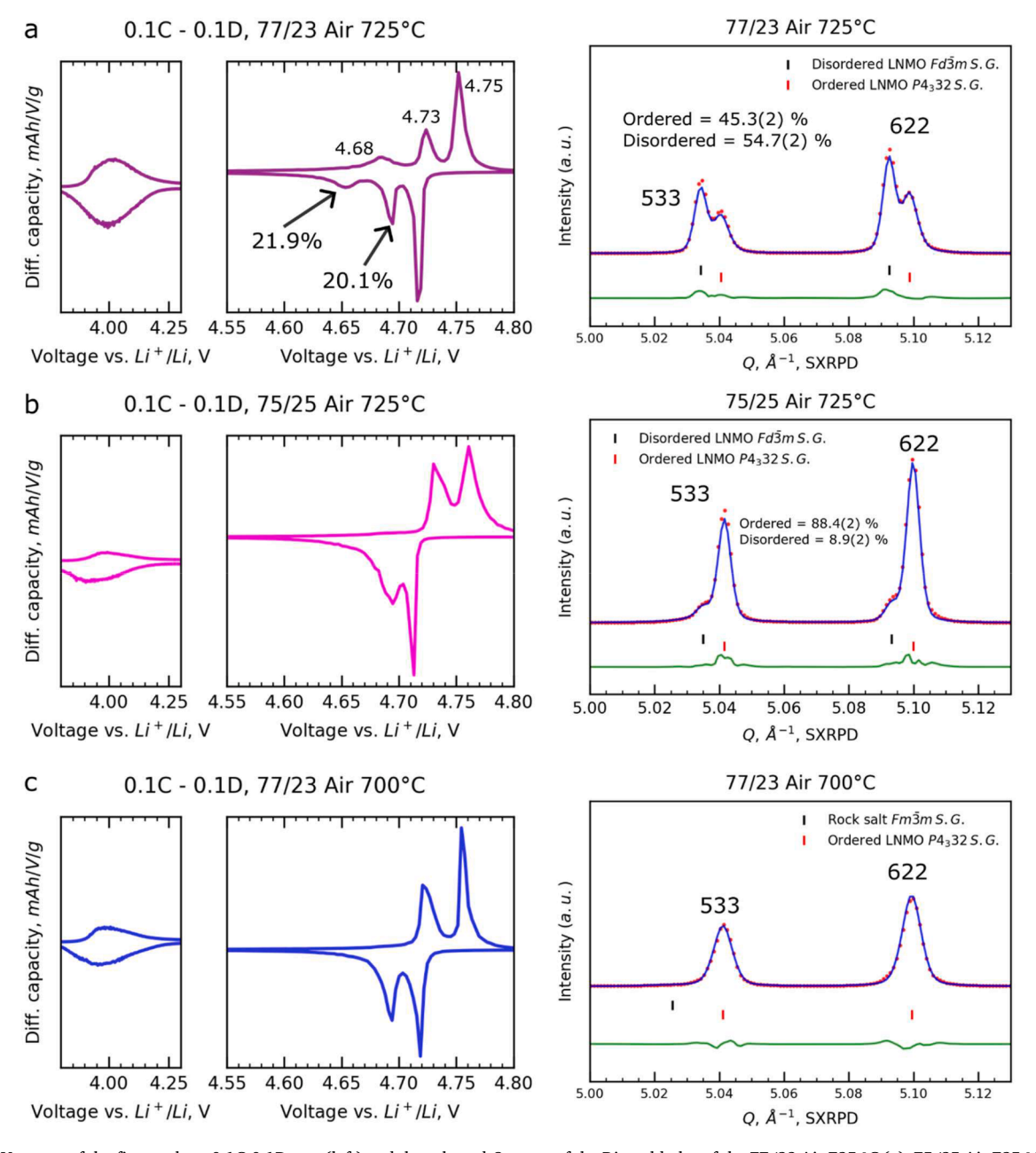


Fig. 9. dQ/dV curves of the first cycle at 0.1C-0.1D rate (left) and the selected Q-range of the Rietveld plot of the 77/23 Air 725 °C (a), 75/25 Air 725 °C (b) and 77/23 Air 700 °C (c) samples.

absent on the dQ/dV curve of the 75/25 Air 725 °C sample (Fig. 9b), which also contains both ordered and disordered LNMO spinel phases, but the amount of the disordered phase is significantly smaller compared to that in the 77/23 Air 725 °C sample. Thus, we can conclude that the additional process at \approx 4.68 V on the dQ/dV curve of the 77/23 Air 725 °C sample corresponds to the disordered LNMO spinel phase. In samples where no peak splitting is observed in the SXRPD patterns, this additional process is also absent. For comparison, Fig. 8b presents the dQ/dV curve of the 77/23 Air 700 °C sample.

Given that this additional process occurs at $\approx 4.68~V$, it can be attributed to the Ni $^{3+}$ /Ni $^{2+}$ redox couple. That is, the oxidation of Ni $^{2+}$ cations during charging corresponds to two processes at $\approx 4.68~V$ and $\approx 4.73~V$, while the oxidation of Ni $^{3+}$ occurs at $\approx 4.75~V$. The different oxidation voltages of Ni $^{2+}$ align well with the coexistence of both disordered and ordered LNMO spinel phases and according to the literature [19], Ni $^{2+}$ oxidation occurs at a lower voltage in disordered LNMO compared to ordered LNMO [8,9,20]. In other words, the charge-discharge and dQ/dV curves of the 77/23 Air 725 °C sample can be considered as a combination of the processes occurring in both disordered and ordered LNMO.

Using the data from Table 1 for the 77/23 Air 725 $^{\circ}$ C sample, it is possible to calculate the expected capacity contribution from the Ni³⁺/Ni²⁺ redox couples in both the disordered and ordered LNMO phases. For the disordered phase, a capacity gain of 21.8(7) % is expected, while

for the ordered phase the gain is 21(1) %. In practice, the contribution to the total capacity for the process at \approx 4.68 V is 21.9 %, and for the process at \approx 4.73 V, it is 20.1 %. These values closely match the calculated ones, confirming the validity of the Rietveld refinement results.

To the best of our knowledge, the simultaneous presence of both disordered and ordered LNMO spinel phases in a single sample has not been previously discussed in the literature and consequently, the presence of three processes corresponding to the $\mathrm{Ni^{4+}/Ni^{3+}/Ni^{2+}}$ redox couples has also not been reported. In Fig. 2d in the work of Aktekin et al. [21], we also identified these three processes on the charge-discharge curve of disordered LNMO with Mn/Ni = 78/22. The authors suggested that the additional process might be related to the different arrangement of occupied ν s. vacant Li sites in this voltage range. Unfortunately, the authors did not provide XRPD and/or NPD data for the studied samples, and their determination of the degree of Mn/Ni ordering was based solely on Raman spectroscopy.

3.9. Impact of structural parameters on high-rate performance of LNMO

The relationships between discharge capacity at 0.1D and 3D rates, the 3D/0.1D ratio, and the lattice parameter of the LNMO spinel phase, the size of the ordered domains, and the ordering parameter are shown in Fig. 10. The corresponding charge-discharge curves can be found in

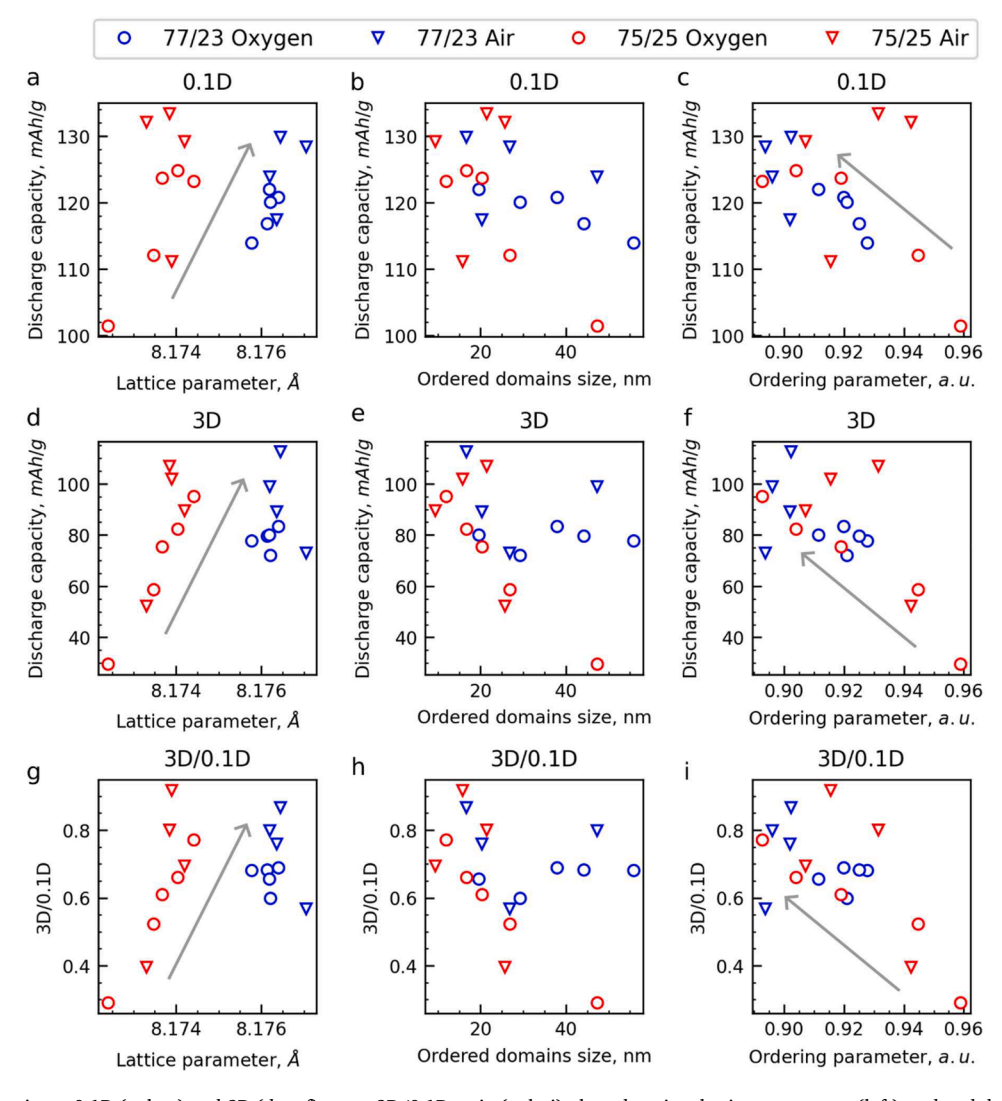


Fig. 10. Discharge capacity at 0.1D (a, b, c) and 3D (d, e, f) rates, 3D/0.1D ratio (g, h, i) plotted against lattice parameters (left), ordered domain size (middle) and the ordering parameter (right) in the LNMO phase.

Fig. 7 and Figure S12. As noted earlier, within the 77/23 and 75/25 sample series, the lattice parameters are similar within the margin of error. Nevertheless, an increase in discharge capacities and the 3D/0.1D ratio is observed with a rise in the average values of the lattice parameter (Fig. 10a, d, g).

As discussed earlier, lattice parameter of the LNMO spinel phase is strongly influenced by its chemical composition – a higher Mn content results in larger lattice parameters.

Therefore, materials with a higher Mn content in the LNMO spinel phase demonstrate more favorable electrochemical performance. Similar results were also obtained in our previous work [13].

A less straightforward relationship is observed when comparing electrochemical performance with the size of the ordered domains and the ordering parameter. It can be seen that the materials exhibiting the most favorable performance are those with smaller domain sizes and lower ordering parameters (Fig. 10b, c, e, f, h, i). Within the 77/23 sample series (blue points in Fig. 10), it appears that the ordering parameter has a more pronounced effect.

It is also worth noting that in our previous study [13], we synthesized two samples with identical ordering parameters and compositions but with more than a fivefold difference in the size of the ordered domains (Samples 77/23 Air and 77/23 Oxygen in [13], both with the similar Mn/Ni ratio of 77/23). The electrochemical performance of these two samples, within the error bar, was effectively the same. Therefore, considering the results of the present study, we conclude that the ordering parameter plays a more significant role than size of the ordered domains in determining the electrochemical performance of LNMO materials.

In conclusion, while we observe a correlation between high-rate performance and the ordering parameter, the combined results from this and our previous work [13] suggest that a slight excess of Mn in the LNMO spinel phase is ultimately the key factor governing electrochemical performance at high rates. It is the Mn content in the LNMO spinel phase that controls the ordering parameter – the degree of Mn/Ni ordering between the 4b and 12d sites.

4. Conclusions and perspectives

In this work, we extensively used NPD to study the impact of the Mn/Ni ratio on Mn/Ni ordering in LNMO. The *in situ* temperature-controlled NPD experiments, along with the SXRPD and NPD studies of LNMO samples with Mn/Ni ratios of 75/25 and 77/23, prepared in air and oxygen atmospheres, clearly demonstrate that the degree of Mn/Ni ordering between the 4b and 12d sites depends on the Mn content in the crystal structure. An increase in the Mn content decreases the Mn/Ni ordering, this Mn content being controlled via the global pristine Mn/Ni ratio in the sample and the annealing conditions. *Re*-annealing disordered LNMO samples in an oxygen atmosphere facilitates the oxygen intake, reducing the Mn content. Additionally, within the temperature range of 600–725 °C, increasing the annealing temperature leads to a higher degree of Mn/Ni ordering.

The approach using HR-STEM followed by FFT image processing allowed us to examine the Mn/Ni ordering at the particle level in a series of LNMO samples prepared within the $600-700\,^{\circ}\text{C}$ range. We found that nanosized, irregularly-shaped ordered domains are homogeneously distributed throughout particles and are separated by disordered areas. As the annealing temperature increases, the size of these domains also increases. Notably, the domain sizes obtained from HR-STEM data correspond well with those derived from Rietveld refinements of NPD patterns, confirming the validity of the structural models used in the Rietveld refinements.

Our structural and electrochemical results from this and our previous study [13] suggest that a slight excess of Mn in almost stoichiometric LNMO promotes the formation of samples with high phase purity and superior high-rate electrochemical performance. These materials can still be described as ordered LNMO; however, at the single-particle level,

a mosaic-like distribution of ordered domains separated by disordered regions is observed. This slight excess of Mn also induces partial Mn/Ni disorder between the 4b and 12d sites. We therefore propose that this mosaic domain structure, together with the partial Mn/Ni cation mixing, high phase purity, and improved electronic conductivity [22], collectively contribute to the enhanced performance observed in Mn-rich LNMO.

One remaining open question concerns the long-term cycling stability of Mn-rich LNMO. It is well known that Mn-rich positive electrode materials are prone to parasitic processes such as Mn dissolution into the electrolyte during cycling. However, strategies such as the use of advanced electrolytes and protective surface coatings may mitigate these effects. To fully assess the impact of slight Mn excess on cycling stability of ordered LNMO samples, future research should focus on long-term electrochemical testing of well-characterized Mn-rich LNMO materials in full-cell configurations. Such studies may help identify an optimal balance between Mn content and long-term stability, guiding the development of best-performing LNMO materials.

CRediT authorship contribution statement

Ilia Tertov: Writing - review & editing, Writing - original draft. Visualization, Validation, Methodology, Investigation, Formal analysis, Data curation, Conceptualization. Dmitry Chezganov: Writing - review & editing, Validation, Methodology, Investigation, Formal analysis, Data curation. Emmanuelle Suard: Writing - review & editing, Validation, Supervision, Methodology, Investigation, Funding acquisition, Formal analysis, Data curation, Conceptualization. Mylène Hendrickx: Writing - review & editing, Validation, Methodology, Investigation, Formal analysis, Data curation. Thomas Hansen: Writing – review & editing, Validation, Supervision, Methodology, Investigation, Funding acquisition, Formal analysis, Data curation, Conceptualization. François Fauth: Writing - review & editing, Methodology, Investigation, Formal analysis, Data curation. François Weill: Writing - review & editing, Validation, Methodology, Investigation, Formal analysis, Data curation. Pierre-Etienne Cabelguen: Writing - review & editing, Validation, Supervision, Methodology, Investigation, Funding acquisition, Conceptualization. Christian Masquelier: Writing - review & editing, Validation, Supervision, Methodology, Investigation, Funding acquisition, Conceptualization. Laurence Croguennec: Writing - review & editing, Validation, Supervision, Methodology, Investigation, Funding acquisition, Formal analysis, Conceptualization.

Declaration of competing interest

We state that there is no conflict of interest regarding this article ENSM 104,359 "Phase Equilibrium during the Synthesis of $\text{LiNi}_{0.46}\text{Mn}_{1.54}\text{O}_4$: Comprehensive X-ray & Neutron Powder Diffraction Study" by Ilia Tertov, François Fauth, Emmanuelle Suard, Thomas Hansen, François Weill, Pierre-Etienne Cabelguen, Christian Masquelier, and Laurence Croguennec.

Acknowledgements

The authors thank Emmanuel Petit, Cathy Denage, Jacob Olchowka, Jérôme Kalisky and Eric Lebraud from ICMCB, Alain Daramsy and Ludovic Gendrin from ILL, and Alexander Missyul from ALBA for their technical support. The authors acknowledge ILL (Grenoble, France) for neutron powder diffraction experiments on the D20 beamline (DOI:10.5291/ILL-DATA.5-24-692) and D2B beamline (DOI:10.5291/ILL-DATA.5-24-691), ALBA (Barcelona, Spain) for synchrotron X-ray powder diffraction experiments on the MSPD beamline (proposal 2022097144). They thank the European Union's Horizon 2020 research and InnovaXN programme under the Marie Skodowska-Curie grant agreement No. 847439 and ILL for the funding of I. Tertov PhD thesis, as well as Umicore, the Région Nouvelle Aquitaine and the French National

Research Agency (STORE-EX Labex Project ANR-10-LABX-76-01) for the financial support of their research.

Supplementary materials

Supplementary material associated with this article can be found, in the online version, at doi:10.1016/j.ensm.2025.104359.

Section 'In situ temperature-controlled NPD of LiNi0.46Mn1.54O4 and LiNi0.5Mn1.5O4'

The detailed description of the Rietveld refinement procedure of the pristine 77/23 and 75/25 samples and corresponding Rietveld plots after refinements of SXRPD and NPD patterns. The contour plots representing evolution of NPD patterns during *in situ* experiments. The detailed description of the Rietveld refinement procedure of NPD patterns collected during *in situ* experiments.

Sections 'Comprehensive structural investigation of the series of 77/23 and 77/25 samples' and 'Electrochemical study'

SXRPD and NPD patterns of the 77/23 Air, 77/23 Oxygen, 75/25 Air and 75/25 Oxygen series of samples, and corresponding Rietveld plots after combined refinement of SXRPD and NPD patterns. The schematic representation of the HR-STEM study coupled with FFT. NPD patterns, and corresponding Rietveld plots after refinements of the SXRPD and NPD patterns of the 77/23 Air 725 $^{\circ}\mathrm{C}$ and 75/25 Air 725 $^{\circ}\mathrm{C}$ samples. Charge-discharge curves at 0.25C-3D rates for the 77/23 Air, 77/23 Oxygen, 75/25 Air and 75/25 Oxygen series of samples.

Data availability

Data will be made available on request.

References

- [1] G. Liang, V.K. Peterson, K.W. See, Z. Guo, W.K. Pang, Developing high-voltage spinel LiNiO.5Mn1.5O4 cathodes for high-energy-density lithium-ion batteries: current achievements and future prospects, J. Mater. Chem. A 8 (2020) 15373–15398, https://doi.org/10.1039/D0TA02812F.
- [2] D. Pasero, N. Reeves, V. Pralong, A.R. West, Oxygen nonstoichiometry and phase transitions in LiMn1.5Ni0.5O4 – δ, J. Electrochem. Soc. 155 (2008) A282, https:// doi.org/10.1149/1.2832650.
- [3] L. Cai, Z. Liu, K. An, C. Liang, Unraveling structural evolution of LiNi0.5Mn1.5O4 by in situ neutron diffraction, J. Mater. Chem. A 1 (2013) 6908, https://doi.org/ 10.1030/r3tr00145b
- [4] M. Kunduraci, G.G. Amatucci, Effect of oxygen non-stoichiometry and temperature on cation ordering in LiMn2−xNixO4 (0.50≥x≥0.36) spinels, J. Power Sources 165 (2007) 359–367, https://doi.org/10.1016/j.jpowsour.2006.11.051.
- [5] J. Cabana, M. Casas-Cabanas, F.O. Omenya, N.A. Chernova, D. Zeng, M. S. Whittingham, C.P. Grey, Composition-structure relationships in the Li-Ion battery electrode material LiNi0.5Mn1.5O4, Chem. Mater. 24 (2012) 2952–2964, https://doi.org/10.1021/cm301148d.
- [6] L. Boulet-Roblin, C. Villevieille, P. Borel, C. Tessier, P. Novák, M.Ben Yahia, Versatile approach combining theoretical and experimental aspects of raman spectroscopy to investigate battery materials: the case of the LiNi0.5Mn1.5O4 spinel, J. Phys. Chem. C 120 (2016) 16377–16382, https://doi.org/10.1021/acs. jpcc.6b04155.

- [7] G. Oney, J. Serrano-Sevillano, M. Ben-Yahia, J. Olchowka, E. Suard, F. Weill, A. Demortiere, M. Casas-Cabanas, L. Croguennec, D. Carlier, Identification of degree of ordering in spinel LiNi0.5Mn1.5O4 through NMR and raman spectroscopies supported by theoretical calculations, SSRN Electron. J. (2024), https://doi.org/10.2139/ssrn.4711856.
- [8] L. Wang, H. Li, X. Huang, E. Baudrin, A comparative study of Fd-3m and P4332 "LiNi0.5Mn1.5O4, Solid State Ionics 193 (2011) 32–38, https://doi.org/10.1016/j. sci. 2011.04.007
- [9] M. Casas-Cabanas, C. Kim, J. Rodríguez-Carvajal, J. Cabana, Atomic defects during ordering transitions in LiNi0.5Mn1.5O4 and their relationship with electrochemical properties, J. Mater. Chem. A 4 (2016) 8255–8262, https://doi. org/10.1039/c6TA00424E
- [10] J.-H. Kim, A. Huq, M. Chi, N.P.W. Pieczonka, E. Lee, C.A. Bridges, M.M. Tessema, A. Manthiram, K.A. Persson, B.R. Powell, Integrated nano-domains of disordered and ordered spinel phases in LiNi0.5Mn1.5O4 for Li-Ion batteries, Chem. Mater. 26 (2014) 4377–4386, https://doi.org/10.1021/cm501203r.
- [11] B. Aktekin, M. Valvo, R.I. Smith, M.H. Sørby, F. Lodi Marzano, W. Zipprich, D. Brandell, K. Edström, W.R. Brant, Cation ordering and oxygen release in LiNi0.5-xMn1.5+xO4-y (LNMO): in Situ neutron diffraction and performance in li ion full cells, ACS Appl. Energy Mater. 2 (2019) 3323–3335, https://doi.org/10.1021/acsaem.8b02217.
- [12] N. Emery, A. Bhatia, Y. Ghaleb, A.O. Mitrushchenkov, C. Léonard, J.-P. Pereira-Ramos, R. Baddour-Hadjean, R.I. Smith, Short-range to long-range Ni/Mn order in LiMn2-xNixO4 (0.38 $\leq x \leq$ 0.50) positive electrode materials: a gradual temperature-driven sublattice disorder through antiphase boundary defects, Chem. Mater. 34 (2022) 3152–3167, https://doi.org/10.1021/acs.chemmater.1c04281.
- [13] I. Tertov, H. Kwak, E. Suard, P.-E. Cabelguen, S. Kumakura, F. Fauth, T. Hansen, C. Masquelier, L. Croguennec, Impact of Mn/Ni and Li/(Mn+Ni) ratios on phase equilibrium and electrochemical performance of the high voltage spinel LiNio.5Mn1.5O4, J. Power Sources 623 (2024) 235447, https://doi.org/10.1016/j.jpowsour.2024.235447.
- [14] F. Fauth, R. Boer, F. Gil-Ortiz, C. Popescu, O. Vallcorba, I. Peral, D. Fullà, J. Benach, J. Juanhuix, The crystallography stations at the Alba synchrotron, Eur. Phys. J. Plus 130 (2015) 160, https://doi.org/10.1140/epip/i2015-15160-y.
- [15] J. Rodríguez-Carvajal, Recent advances in magnetic structure determination by neutron powder diffraction, Phys. B 192 (1993) 55–69, https://doi.org/10.1016/ 0921-4526(93)90108-I.
- [16] I. Lobato, T. Friedrich, S. Van Aert, Deep convolutional neural networks to restore single-shot electron microscopy images, Comput. Phys. (2023), https://doi.org/ 10.48550/ARXIV.2303.17025.
- [17] R. Ishikawa, N. Shibata, Y. Ikuhara, Three-dimensional crystal defect imaging by STEM depth sectioning, Chin. Phys. B 33 (2024) 086101, https://doi.org/10.1088/ 1674-1056/ad4ff9.
- [18] J. Song, D.W. Shin, Y. Lu, C.D. Amos, A. Manthiram, J.B. Goodenough, Role of oxygen vacancies on the performance of LiNi[0.5-xMn1.5+x]O4 (x = 0, 0.05, and 0.08) spinel cathodes for lithium-ion batteries, Chem. Mater. 24 (2012) 3101–3109, https://doi.org/10.1021/cm301825h.
- [19] G. Liang, V.K. Peterson, K. Wai See, Z. Guo, W.K. Pang, Developing high-voltage spinel LiNi 0.5 Mn 1.5 O 4 cathodes for high-energy-density lithium-ion batteries: current achievements and future prospects, J. Mater. Chem. A 8 (2020) 15373–15398. https://doi.org/10.1039/D0TAQ2812F.
- [20] P. Stüble, V. Mereacre, H. Geßwein, J.R. Binder, On the composition of LiNi0.5Mn1.5O4 cathode active materials, Adv. Energy Mater 13 (2023) 2203778, https://doi.org/10.1002/aenm.202203778.
- [21] B. Aktekin, F. Massel, M. Ahmadi, M. Valvo, M. Hahlin, W. Zipprich, F. Marzano, L. Duda, R. Younesi, K. Edström, D. Brandell, How Mn/Ni ordering controls electrochemical performance in high-voltage spinel LiNi0.44Mn1.5604 with fixed oxygen content, ACS Appl. Energy Mater. 3 (2020) 6001–6013, https://doi.org/10.1021/acsaem.0c01075.
- [22] M. Kunduraci, J.F. Al-Sharab, G.G. Amatucci, High-power nanostructured limn2-xnixo4 high-voltage lithium-ion battery electrode materials: electrochemical impact of electronic conductivity and morphology, Chem. Mater. 18 (2006) 3585–3592, https://doi.org/10.1021/cm060729s.